UNIVERSIDADE FEDERAL DE SÃO CARLOS

CENTRO DE CIÊNCIAS EXATAS E DE TECNOLOGIA

PROGRAMA DE PÓS-GRADUAÇÃO EM FÍSICA

PhD Dissertation

DIELECTRIC AND ELASTIC RESPONSE OF PEROVSKITES: MODELLING AND SIMULATION

Presented by

Rolando Placeres Jiménez

Dissertation submitted to the Department of Physics,
of theUniversidade Federal de São Carlos –DF/UFSCar
In partial fulfillment of the requirements for the degree
of Doctor of Philosophy.

Advisor: Prof. Dr. José Pedro Rino

Co-advisor: Prof. Dr. José Antonio Eiras

UFSCar-São Carlos
December 2013

Ficha catalográfica elaborada pelo DePT da Biblioteca Comunitária/UFSCar

P697de

Placeres Jiménez, Rolando.
Dielectric and elastic response of perovskites : modelling and simulation / Rolando Placeres Jiménez. -- São Carlos : UFSCar, 2013.
75 f.

Tese (Doutorado) -- Universidade Federal de São Carlos, 2013.

1. Física da matéria condensada. 2. Ferroelétricos. 3. Dinâmica molecular. 4. Resposta dielétrica não-linear. 5. *Perovskitas*. I. Título.

CDD: 530.41 (20ª)

Rolando Placeres Jimenez

Tese de doutorado submetida à Coordenação do Programa de Pós-Graduação em Física, da Universidade Federal de São Carlos, como requisito parcial para a obtenção do título de doutor em ciências.

Aprovado em: 09 de Dezembro de 2013

BANCA EXAMINADORA

Prof. Dr. José Pedro Rino (Orientador)
Universidade Federal de São Carlos - DF

Prof. Dr. José Antônio Eiras
Universidade Federal de São Carlos - DF

Prof. Dr. Victor Lopez Richard
Universidade Federal de São Carlos – DF

Prof. Dr. Alexandre Souto Martinez
Universidade de São Paulo - FFCL

Prof. Dr. Valmor Mastelaro
Universidade de São Paulo - IFSC

Prof. Dr. Alex Antonelli
Universidade Estadual de Campinas – IFGW

ACKNOWLEDGEMENTS

I would like to thank to the Professors José P. Rino and José A. Eiras for giving me the opportunity to work in their research groups, as well as for their guidance and patience through these four years. Sharing and discussing ideas with them were always inspiring. I want to express my gratitude to the colleagues and friends of the Physics Department that made life at work so much easier and more fun. Thanks to my colleagues Luis G. Vieira Gonçalves, Bárbara Fraygola and André M. Gonçalves, with whom I had the pleasant opportunity to work.

I knowledge the financial support from the Centro Latinoamoericano de Física (CLAF) and the Brazilian agency CNPq.

SUMMARY

In this thesis the elastic and electric response of perovskites are studied. Perovskites are widely used in technical applications, being fundamental in electronic and in the relatively new field of nanoelectronics. They also pose a very interesting challenge from the theoretical point of view due to a number of unresolved questions. Two problems are treated using different theoretical approaches. The first problem is focused on the anomalous elastic behavior of the $CaTiO_3$ around 200 K. Molecular dynamics simulation is used to simulate the elastic response of a mono-domain and a poly-domain configuration of $CaTiO_3$ using the Vashishta-Rahman interatomic potential. The anomalous behavior is reproduced but no structural change was detected. Using nonlinear time series analysis it is shown that such anomalies are dynamic and are generated by domain walls motion. The second problem treated is more general and concerns the nonlinear dielectric response. Two models of domain wall motion are proposed with which it is possible to reproduce the effects of electric field strength and frequency and transient effects. In the first model, the domain wall is considered as a stretched membrane. Dispersion relationships and dependence of permittivity with electric field are derived. With this model it is possible to reproduce the hysteretic behavior of the permittivity versus electric field. This model correctly explains the effect of grain size on the dielectric response. The second model considers that the domain wall behaves as a rigid body moving under the action of a potential field in a dissipative medium. Assuming that the dielectric permittivity follows the dependence $\varepsilon' \propto 1/(\alpha + \beta E^2)$ the exact expression for the effective potential is obtained. Simulations of polarization current correctly predict a power law. The model is extended to poled samples allowing the study of nonlinear dielectric permittivity under subswitching electric fields. These simple models for domain wall motion could be very useful to obtain information of microscopic parameters from dielectric measurements. They could also be very helpful to separate conductive currents from polarization mechanisms, especially in ferroelectric thin films.

RESUMO

Nesta tese é estudada a resposta elástica e elétrica das perovskitas. As perovskitas são amplamente utilizadas em aplicações técnicas, sendo fundamental na eletrônica e no campo relativamente novo da nanoeletrônica. Elas representam um desafio muito interessante do ponto de vista teórico, devido a uma série de questões ainda não resolvidas. Dois problemas são tratados com diferentes abordagens teóricas. O primeiro problema é focado no comportamento elástico anômalo do CaTiO3 em torno de 200 K. A dinâmica molecular é usada para simular a resposta elástica de uma configuração de monodomínio e polidomínio de $CaTiO_3$ usando o potencial interatômico Vashishta - Rahman. O comportamento anômalo é reproduzido, mas nenhuma mudança estrutural foi detectada. Utilizando a análise não-linear de séries temporais é mostrado que tais anomalias são dinâmicas e são geradas pelo movimento das paredes de domínio. O segundo problema tratado é mais geral e refere-se à resposta dielétrica não-linear. Dois modelos para o movimento de paredes de domínio são propostos com o qual é possível reproduzir os efeitos da intensidade do campo elétrico e frequência, e comportamento transientes. No primeiro modelo, a parede de domínio é considerada como uma membrana esticada. As relações de dispersão e dependência da permissividade com campo elétrico são derivadas. Com este modelo é possível reproduzir o comportamento histerético do permissividade em função do campo elétrico. O modelo explica corretamente o efeito do tamanho de grão na resposta dielétrica. O segundo modelo considera que a parede do domínio comporta-se como um corpo rígido que se move sob a ação de um campo de forças de potencial num meio com dissipação. Supondo que a constante dielétrica segue a dependência $\varepsilon' \propto 1/(\alpha + \beta E^2)$ é obtida a expressão exacta do potencial efectivo. Simulações de corrente de polarização preve corretamente uma lei de potência. O modelo é estendido para amostras polarizadas permitindo o estudo da permissividade dielétrica não-linear para campos elétricos de subswitching. Estes modelos simples para o movimento da parede de domínio podem ser muito úteis para obter informação dos parâmetros microscópicos a partir de medições dielétricas. Também poderiam ser muito úteis para separar correntes condutoras de mecanismos de polarização, especialmente em filmes finos ferroelétricos.

LIST OF FIGURES

LIST OF TABLES

CONTENTS

Chapter 1. Introduction

Different approaches can be used to investigate a given phenomenon. The most common one is the experiment, a technique that has been used by humans for a long time. Through experiments the observer can get a representation of the process of interest, since an experiment is per definition carried out under controlled and reproducible circumstances. Based on experiments hypotheses can be concluded, and laws and theories can be formulated. The second approach to investigate a phenomenon is simulation. A simulation is the imitation of a real system. In other words reality is modeled in a representative system.

Simulations are applied when conducting experiments is not possible, unethical or tedious and time consuming. But in the cases when reality is correctly reproduced by simulation still experiments are needed to validate and confirm results gathered from simulations.

Computer simulations have become a very frequently used tool, not only in science, but in many different fields, such as risk management, stock-market prediction, the development of cars and planes, drug discovery and many more.

Rational design of material is possible thanks to present capability to model and simulate. Rather than improving existing or developing novel materials by trial and error, the properties of novel materials can be fine-tuned for a particular application by taking advantage of understanding how microscopic structure affect the macroscopic response.

This thesis focuses on the properties of perovskites materials. Specifically, the electric and elastic behaviors of these materials are investigated. Theoretical and computational tool are employed, providing insight into the microscopic structure and their response to external perturbations at a level of detail that it is not possible to achieve experimentally. The combination of microscopic modeling and computer simulations allow a better understanding of how determined structures give rise to certain physics properties, enabling the design of new materials with the desired properties.

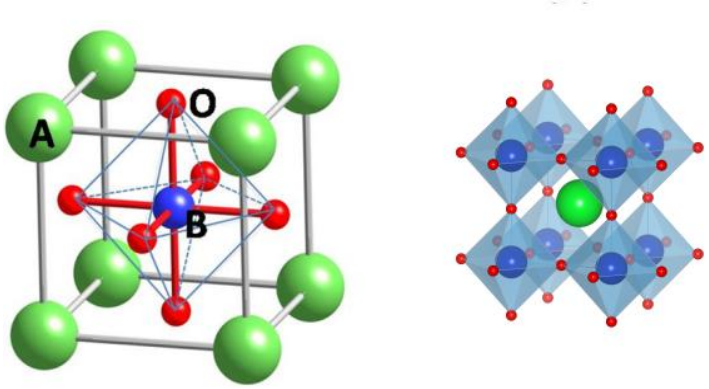

Figure 1.1 Perovskite structure ABO_3, green spheres represent the A^{2+} cations, blue spheres represent the B^{4+} cations, and red spheres represent oxygen anions forming an octahedra.

The perovskite oxides (formula ABO_3) are a class of material of fundamental scientific interest as well as a varied of technological applications [1-3]. They display a variety of interesting properties such as piezoelectricity, pyroelectricity, ferroelectricity and ferroelasticity, among others.

The name of perovskite is used to designate the material that share a similar structure of $CaTiO_3$. The $CaTiO_3$ was the first perovskite mineral discovered, reason for which is known as the father of the perovskites family. Perovskites can adopt various crystal structures of different symmetry, been the simplest cubic symmetry. It consists of A cations on the corners of a cubic unit cell, oxygen anions on the faces, and B cations in the centers, as shown in Figure 1.1. Usually, the cation displacements away from oxygen cage center and the oxygen octahedral rotation occur, given rise lower symmetry structures. The breaking of cubic symmetry is crucial to the occurrence of spontaneous polarization.

Ferroelectric oxides are a subgroup of perovskites oxides that posses a permanent electric dipole. At low temperature spontaneous polarization appears which can be reversed by an applied electric field. The relation between polarization and electric field is nonlinear and hysteretic. When the temperature is raised above the Curie temperature a phase transition (ferroelectric to paraelectric phase) occurs with a sudden disappearance of the spontaneous polarization.

An important characteristic of ferroelectric it is the existence of domain structure. A domain is a region where unit cells share the same or similar polarization direction. Bulk ferroelectrics contain several domains. A ferroelectric domain pattern can be caused or influenced by strain, defects, depolarization field and thermal history.

Even in an ideal crystal, the existence of a domain structure is expected due to the minimization of energy. Usually, neighboring domains could be either antiparallel to each other, or bisects the 90° angle between two domain walls pointing head to tail. The formation of domain walls involved several energetic contributions: the elastic energy of the material, temperature, boundaries, electrostatics interaction, and defects [2].

Motion of domain walls can be pinned by defects. At a certain temperatures threshold ('activation temperature') domain walls have sufficient energy to overcome potential barrier created by defects. The resulting motion of domain walls can be abrupt, i.e., it can form avalanches. From macroscopic point of view, anomalies and instability in physical properties can appear around the temperature of 'activation'.

Domain wall motion has an important contribution to dielectric response and to the nonlinear dielectric properties of ferroelectrics. The understanding and control of the response of nonlinear dielectrics can open new possibilities for technical applications.

The title of this thesis could seem broad or ambitious and, in effect, it is. So, it is important to elucidate the problems and objectives treated here. The content covered consists in two problems. The first concerns with the anomalous elastic behavior observed in the $CaTiO_3$ around 200 K. Classical molecular dynamics simulations are carried out to reproduce the anomalous behavior. The objective is to characterize the anomaly from the dynamical point of view and to show that this phenomenon is not generated by structural changes. Due complex nature of this problem, nonlinear time series analysis is used to reconstruct and characterize the dynamic of the system. This approach by itself constitutes, in certain way, a contribution of this work. The theory of nonlinear time series analysis was developed between the 1980 and the 1990's and it is a powerful theoretical tool to treat complex problem. Unfortunately, in solid state physics it has remained almost ignore up to present days. The methodology used in this problem could be applied in many branches of solid state physics.

The second problem is more general, and it concern with the nonlinear dielectric response of ferroelectrics. The objective is to model and simulate the effect of external electric field (strength and frequency) in the dielectric response. The models developed here are not atomistic; they can be classified as collective motion models and are based in domain structure and the displacement of domain walls. The two models

presented are original contributions to the theory of nonlinear dielectric response and they could be very interesting from both theoretical and practical point of view.

The thesis has the following structure. The principal features of perovskites (structure, electric and mechanic response) are shortly reviewed in Chapter 2. In Chapter 3 the basic concepts of molecular dynamics are outline. Basic concepts of nonlinear time series theory are explained Chapter 4. The anomalous behavior of $CaTiO_3$ is studied in Chapter 5. Finally, nonlinear dielectric response of perovskites is studied in Chapter 6 using collective models for domain wall movement.

Chapter 2. Perovskites: ferroelectric and ferroelastic properties

In this chapter, ferroelectric and ferroelastic properties are discussed, which are commonly observed in perovskites. Phenomenological theory and symmetry detail are covered in many excellent books [4-7]. For this reason, this chapter is limited to a descriptive presentation of the essential concepts of ferroelectricity and ferroelasticity. Other theoretical approaches are discussed in the Chapters 5 and 6.

2.1 Ferroelectricity

Ferroelectrics can be defined as polar materials that posses at least two equilibrium orientation of the spontaneous polarization and in which the spontaneous polarization may be switched between those orientation by an electric field. Most ferroelectrics undergo a structural phase transition from high temperature paraelectric (nonferroelectric) phase into a low temperature ferroelectric phase. The temperature of the phase transition T_c is called the Curie point. Above the Curie point the dielectric permittivity falls off with temperature according to the Curie-Weiss law

$$\varepsilon = \varepsilon_0 + \frac{C}{T - T_0} \tag{2.1}$$

where C is the Curie constant, T_0 ($T_0 \leq T_C$) is the Curie-Weiss temperature. The transition into a ferroelectric phase usually is accompanied by anomalies in the dielectric, elastic, thermal and other properties of the material [2] and with changes in the dimensions of the crystal unit cell. Symmetry of unitary cell in ferroelectric phase is lower than the symmetry of the paraelectric phase.

Most of the ferroelectric materials that are of practical interest have perovskite structure. Perovskites have the general formula ABO_3 where the valence of A cations is from +1 to +3 and of B cations from +3 to +6. The structure, as is shown in Figure 2.1, consist of BO_6 octahedra surrounded by A cations. The lead titanate $PbTiO_3$ is a perovskite which passes from a paraelectric cubic to a ferroelectric tetragonal phase at 490 °C. The spontaneous polarization in $PbTiO_3$ is oriented along the c_T-axis of the tetragonal unit cell, and is due to the shifts of O and Ti ions relative to Pb, Figure 2.1.

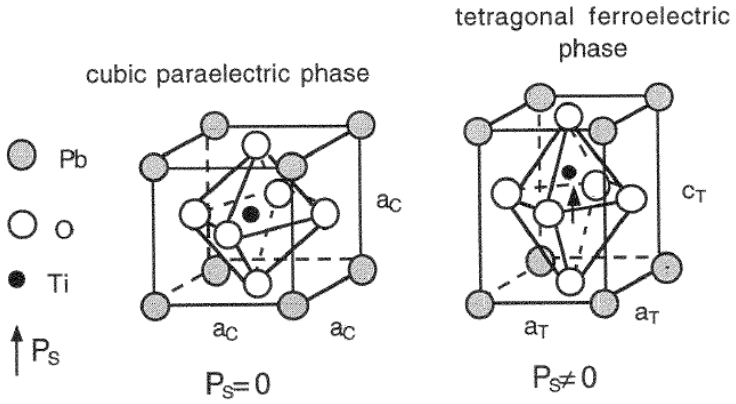

Figure 2.1 Perovskite structure of $PbTiO_3$ which has a cubic structure in the paraelectric phase and tetragonal structure in the ferroelectric phase [2].

The spontaneous polarization in a ferroelectric crystal (or a grain in the case of a ferroelectric film or ceramic) is usually not uniform aligned on whole crystal. The regions of the crystal with uniformly oriented spontaneous polarization are called ferroelectric domains. The interface that separate two domains is call the domain wall. The walls which separate domains with oppositely oriented polarization are called 180° (Figure 2.2a) walls and those which separate regions with mutually perpendicular polarization are called 90° walls (Figure 2.2b).

As the ferroelectric material is cooled through paraelectric-ferroelectric phase transition, domains occur to minimize the electrostatic energy of depolarizing fields and the elastic energy associated with mechanical constrains [4]. The depolarizing field is formed whenever there is a nonhomogeneous distribution of the spontaneous polarization, for example, due to the fall-out of polarization near the surface of the ferroelectric or due to a change in the direction of polarization at grain boundaries. The electrostatic energy associated with the depolarizing field may be minimized if the ferroelectric splits into domains with oppositely oriented polarization or if the depolarizing charge is compensated by electrical conduction through the crystal or by charges from the surrounding (the atmosphere or from the electric circuit to which is connected).

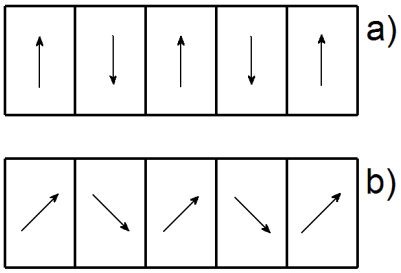

Figure 2.2 Schematic representation of domain structure: a) 180° domains, b) 90° domains.

Depending on the electric and elastic boundaries conditions in a same ferroelectric can be formed by a domain structure of both 90° and 180° walls. 90° and 180° walls are not the unique type of domain walls. In the Pb(Zr, Ti)O_3, for example, posses 180°, 71° and 109° domain walls. The types of domain walls that can appear in a ferroelectric depend on the symmetry of both the paraelectric and ferroelectric phases of the crystal [2, 4].

2.1.1 Poling of ferroelectrics

Ferroelectric grains in ceramics and polycrystalline films are always split into many domains. The spontaneous polarization through the material is random or distribute in some way that the net polarization is zero. Polycrystalline ferroelectrics may be brought into a polar state by applying a strong electric field, which can be combined with elevate temperature. This process, named poling, cannot orient the grains, but can orient domains within individual grains in the direction of the field. A single crystal that does not contain domains is said to be in a single-domain or mono-domain state. Ferroelectric single crystal usually contain many domains, mono-domain state can be achieved by poling.

The polarization after the removal of the field (at zero field) is called remanent polarization P_r. Maximum remanent polarization that may be achieved in a polycrystalline material depends on domain states. The actual remanent polarization is always lower, because many domains cannot be reoriented due to internal stresses and electric fields in grains, and because some domain switch back after the poling field is removed.

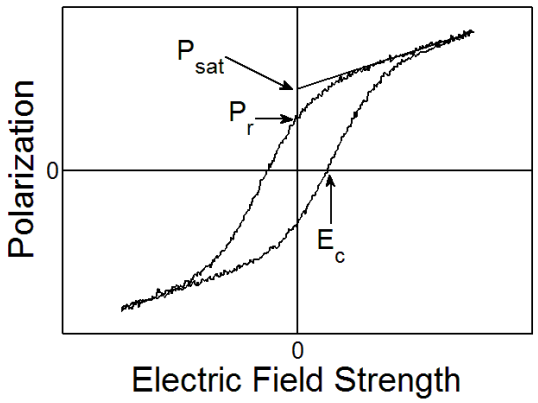

Figure 2.3 Ferroelectric hysteresis loop.

2.1.2 Hysteresis and switching

A distinctive characteristic of ferroelectrics is the occurrence of hysteresis loop (see Figure 2.3) for high alternant electric fields. Hysteresis is a consequence of domain reorientation (switching) in ferroelectrics. Initially the polarization of the material is zero (Figure 2.3). At small electric field the polarization increases linearly with the field amplitude. As the field is increased the polarization of domains with an unfavorable direction of orientation will start to switch in the direction of the field. The polarization response in the region of strong electric field is nonlinear. Once all the domains are aligned the ferroelectric again behaves linear. If the field strength decreases the polarization also decreases, but at zero field the polarization is nonzero. To reach a zero polarization state the field must be reversed. The field necessary to bring the polarization to zero is called the coercive field E_c and the value of polarization at zero field remanent polarization P_r. Further increase of the field in the negative direction will cause a new alignment of dipoles and saturation. The saturation polarization P_{sat} is taken as the intercept of the polarization axis with the extrapolated segment of linear response at high electric field. Notice that in polycrystalline ferroelectrics the saturation polarization is lower than the spontaneous polarization.

The problem of polarization switching is complex and there does not seem to be a universal mechanism which would be valid for polarization reversal in all ferroelectrics [2]. The polarization reversal takes place by growth of existing antiparallel domains, by domain wall motion, and by nucleation and growth of new domains.

2.1.3 Domain wall contribution to ferroelectric properties

There are five mechanisms of polarization which can contribute to the dielectric response:

1. *Electronic polarization* this mechanism exist in all dielectrics. It occurs due the displacement of negative charged electron shell against the positive charged core. The electronic polarizability (α_{elect}) is approximately proportional to the volume of the electron shell and in general is independent of the temperature.
2. *Ionic polarization* is observed in ionic crystals and is the result of the displacement of positive and negative ions under an applied electric field.
3. *Orientation polarization* describes the alignment of permanent dipoles. An electric field generates a preferred direction for the dipoles, while the thermal movement of the atoms perturbs the alignment.
4. *Space charge polarization* could exist in dielectric materials which show spatial inhomogeneities of charge carrier density. Space charge polarization effect occurs in ceramics with electrically conducting grains and insulating grain boundaries (so-called Maxwell-Wagner polarization).
5. *Domain wall polarization* is decisive in ferroelectric materials and contributes to the overall dielectric response. The motion of domain wall that separates regions of different oriented polarization takes place by the fact that favored oriented domains with respect to the applied field tends to grow.

The total polarization of dielectric material results from all the contributions discussed above. The contribution from the lattice (electronic and ionic polarizations) is called intrinsic contribution, in contrast to the extrinsic contributions (orientation, space charge and domain wall polarizations).

Ferroelectric domain walls may move under weak and moderate (subswitching) fields, either by vibration or bending around an equilibrium position or by small jumps into new equilibrium state. The displacement of domain walls at subswitching electric fields has a great influence on the dielectric and mechanical properties of ferroelectric materials. Small displacements of all types of domain will affect the polarization of the material. Movement of domain walls at weak to moderate fields is one of the most important extrinsic contributions to the dielectric properties of ferroelectrics.

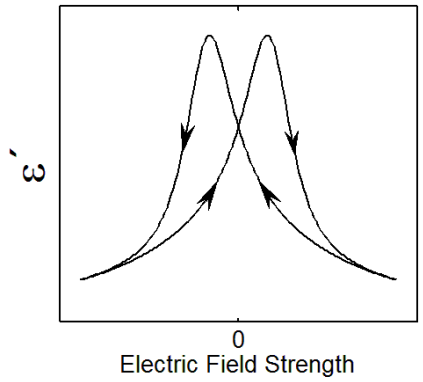

Figure 2.4 Dielectric permittivity as function of the electric field strength.

Displacement of domain walls also contributes to the dielectric and mechanical losses of ferroelectric materials. The grain size, dopants, crystallographic orientation and crystal structure, external stresses, electric fields, preparation conditions may through various processes affect domain wall displacement.

2.1.4 Effect of external electric field

Dielectric permittivity versus electric field (or capacitance versus voltage) loops are commonly used in the characterization of ferroelectrics. A typical behavior of the ε(E) (or CV) curve is shown in Figure 2.4. The measurement is usually performed applying simultaneously a constant electric field (called bias field) and an alternate small amplitude electric field.

Initially, the permittivity tends to rise as the electrical field increases. The curve ε(E) reaches a maximum for a value of electric near to the value of coercive field of the hysteresis loop. At high bias field, the permittivity decreases. This diminution of the permittivity is due to (i) the decrease of the number of domain as they become aligned with the field and (ii) the diminution of the domain wall movement at elevate bias field. It is possible that small oscillations of domain wall occur even at very large electric field, contributing to the dielectric field but reduced in contrast with respect to low bias field. This problem is studied in the Chapter 6.

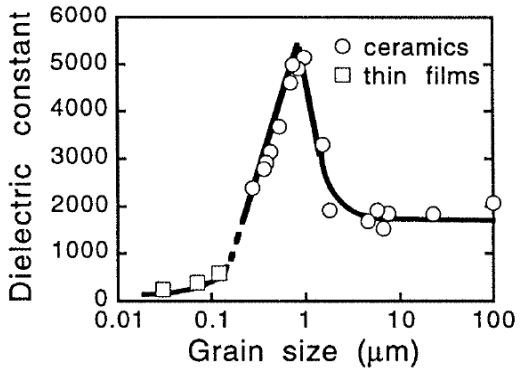

Figure 2.5 Dielectric constant of BaTiO3 ceramics and thin films for samples with different grain size [2].

2.1.5 Size effects

It is well known that microstructure of polycrystalline ferroelectrics affect the dielectric response. An important example is the grain-size dependence of dielectric permittivity in barium titanate ceramics [8-10] and thin films [9] (Figure 2.5). Even after more than 40 year of research the origins of the high permittivity in fine-grained barium titanate ceramics are still not completely understood. This problem is treated qualitatively in Chapter 6 where is explained the decrease of permittivity with the decrease of domain (grain) size.

2.1. 6 Domain wall pinning

Real ferroelectrics always contain electrical and elastic defects and imperfections that can interfere in a number of ways with domain walls movement and polarization within individual domains. In many cases defects inhibit domain wall movement. It is said that domain walls become pinned or clamped by the defects and imperfections. Some common domain wall pinning defects include oxygen vacancies and electrons trapped in the domain wall area [2].

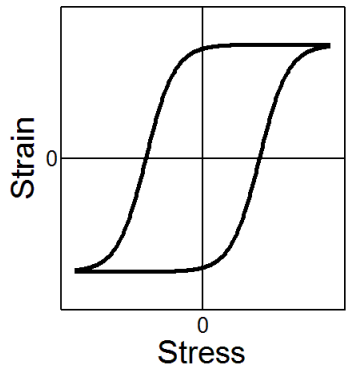

Figure 2.6 Ferroelastic hysteresis loop.

2.2 Ferroelasticity

When stresses are applied to a ferroelastic material the curve strain-stress describes a hysteresis loop (Figure 2.6), analogous as is observed in ferroelectrics and ferromagnetic materials [11]. Many ferroelectrics and ferromagnetic material are ferroelastic. The hysteresis is the result of the mechanical switching between at least two orientation states of a crystal by external stress. Most ferroelastic materials show ferroelastic-paraelastic phase transition.

The experimental observation of ferroelastic hysteresis with any acceptable degree of accuracy results difficult. The essential property that characterizes ferroelasticity is the occurrence of spontaneous strain, i.e., a deformation of the crystal which has to have at least two orientations between which switching may occur. The spontaneous strain is usually accompanied by an anomaly of the elastic modulus, which is often taken as a signal of a ferroelastic phase transition.

There are materials with large elastic anomaly and/or spontaneous strain but hysteresis is not observed. In these cases the material is classified as coelastic [11]. Some coelastic when are doped with atoms that acts as nucleation centers for twin boundaries becomes ferroelastics.

Similar to ferroelectrics, in ferroelastics the domain structure can adopt different patterns. The atomic structure inside the wall is not the same as in the bulk. Interesting properties can emerge in the walls that do not exist anywhere else in the structure [11]. The research in this area is termed domain boundary engineering. Two different approaches dominate this field. In the first approach the chemical composition of the wall is modified by local doping. This is possible because the chemical potential of

the wall is different from the bulk. Dopants or defects are attracted to (or repelled by) the wall. The second approach directly tackles the structural configuration of the wall structure. For example in ionic perovskites ($SrTiO_3$, $CaTiO_3$) the octahedron tilts slightly in the ferroelastic phase, the octahedron generally does not show a ferroelectric displacement of its central position. When the small octahedron rotation is prevented, a ferroelectric displacement is possible (such as in $BaTiO_3$). Octahedral rotations can be suppressed by surface strains or inside twin boundaries. This effect has been observed experimentally in $CaTiO_3$, where the Ti suffers a displacement from the midpoint of the octahedral.

For small forces and low frequencies wall movements appear ballistic. Damping is generated by the emission of phonons and the interaction with defects. Ballistic propagation of domain walls is often superimposed abrupt movements or avalanches. Avalanches in ferroelastic materials have been observed experimentally [12, 13], the energy distribution of jerky movement follows a power law

$$P(E) \sim E^{-\alpha} \tag{2.2}$$

It must point out that other material show similar behavior with power-law dependences also for the size distribution [11, 14, 15]. The occurrence of avalanches has also been confirmed by large-scale molecular dynamics computer simulations [16].The occurrence of abrupt movement of domain walls is consequence of pinning.

Chapter 3. Basic concepts of molecular dynamics

In this chapter are introduced the basic concepts of classical molecular dynamics. Potentials and several thermodynamic ensembles are explained as vital concepts in order to understand the way the molecular dynamics simulations are performed.

3.1 Molecular dynamics simulations

Why to use molecular dynamics simulation? In spite of the recent advances on microscopic imaging the study of atomic structure of perovskites presents big technical challenges. Current process takes places in times scales of picoseconds. In other side, molecular dynamics simulations allow the possibility to reproduces physical condition such as ultrahigh pressures and electric fields that cannot be easily studied by conventional experiments.

The first thing that might be important to mention is that we do classical molecular dynamics. That means quantum effects are not considered, or only in a mean-field manner. Everything that underlies the laws of quantum physics, i.e., the motion of electrons, is neglected. Classical molecular dynamics simulation is the method that dynamically investigates a group of atoms with their positions and velocities evolving with time and can be related to macroscopic properties such as temperature and pressure. In other words, molecular dynamics simulation is the method that computationally helps to build a bridge between the microscopic structure, that we can barely measure, and macroscopic properties with which we can usually describe the tangible world. Following is the simplified description of how the molecular dynamics simulation works.

Molecular dynamics simulation is essentially the solution of Newton's second law or the equation of motion, which for a simple system of atoms, where a specific atom to be studied is denoted as atom k, can be expressed as

$$F_k = m_k \frac{d^2 r_k}{dt^2} \tag{3.1}$$

$$F_k = -\nabla U(r_k) \tag{3.2}$$

where F_k denotes the force exerted on the atom k by all atoms in the system except for itself, m_k and r_k are the mass and position of that atom respectively. Knowing the position of the atom the force is calculated as the gradient of the intermolecular potential $U(r_k)$.

In molecular dynamics simulations the integration is done numerically, for which there are several methods available [17]. At each time step relevant phase variables such as averaged temperatures and pressures can be calculated from updated coordinates and velocities of atoms by statistical physics. For example, in order to obtain the average temperature T from a three-dimensional system with the number atoms of N, the following relation can be utilized:

$$\frac{1}{2}\sum_{j=1}^{N} m_j v_j^2 = \frac{3N}{2} k_B T \tag{3.3}$$

where m_j and v_j are the mass and velocity respectively for an atom j, and k_B is the Boltzmann constant. The pressure can be calculated from the virial expression

$$w = \sum_{j=1}^{N} r_j \cdot F_j \tag{3.4}$$

where F_j is resulting force acting in the particle placed in r_j. Averaging the virial function [17]

$$\langle w \rangle = \lim_{\tau\to\infty} \frac{1}{\tau}\int_0^\tau \sum_{j=1}^{N} m_j r_j \cdot \ddot{r}_j dt \tag{3.5}$$

Integrating by parts and assuming the conservation of angular momentum of the system we obtain that

$$\langle w \rangle = -\lim_{\tau\to\infty} \frac{1}{\tau}\int_0^\tau \sum_{j=1}^{N} m_j \left|\dot{r}_j\right|^2 dt = -3Nk_B T \tag{3.6}$$

The function w can be divided in two components, one due to internal forces f_j resulting from the interaction between the particles, and the component resulting from the action of external forces:

$$\langle w \rangle_{ext} + \langle w \rangle_{int} = -3Nk_B T. \tag{3.7}$$

In a parallelepiped the component $\langle w \rangle_{ext}$ due to hydrostatic pressure is

$$\langle w \rangle_{ext} = -3PV.$$

Thus,

$$\left\langle \sum_{j=1}^{N} r_j \cdot f_j \right\rangle - 3PV = -3Nk_B T \tag{3.8}$$

from which we have that $P = \frac{1}{3V}\left\langle \sum_{j=1}^{N} r_j \cdot f_j \right\rangle - \frac{Nk_B T}{V}$.

It might be of interest to compare the collected data with data from experiment. In an experiment the measured value of an observable or property F is the average ⟨F⟩ over time and space of F that is produced by different molecular configurations. In order to get the right value, F has to be weighted by the probability Γ of a configuration to occur integrated over momenta ($\vec{p}$) and positions ($\vec{r}$),

$$\langle F \rangle = \iint F(r, p)\Gamma(r, p)\mathrm{d}\, r\mathrm{d}p \tag{3.9}$$

In molecular dynamics it can be very difficult to sample all possible states within a single, finite simulation. However, if the configurations that are relevant for the average are properly sampled, ⟨F⟩ can be calculated from this finite set of configurations. The ergodic hypothesis assumes that the relevant configurations are sampled during a molecular dynamics simulation that is long enough. Averages are then calculated with

$$\langle F \rangle_{MD} = \lim_{\tau\to\infty} \frac{1}{\tau}\int_0^\tau F(t)\mathrm{d}t \tag{3.10}$$

with τ being simulation time and t being time.

Calculating properties is what makes comparison to experimental data possible, and thus allows validation of the results of a molecular dynamics simulation.

3.2 Interatomic potential

The interaction between the particles is determined by the potential. The potential of one particle $U(r_k)$ depends of the position r_k of individual particle. It is used to model the interaction of the particle with external fields. Two body potential $U(r_{kj})$ are those in which the interaction depends solely on the distance between the particles $r_{kj} = |r_k - r_j|$, for example Coulomb interaction. Only to mention, there are more complex potentials such as the three body potential. We will restrict to one and two body potentials.

As two body potential we use the Vashishta-Rahman, which have been successfully applied to diverse systems [18-24]. This potential is given by the function

$$U(r_{kj}) = \frac{1}{4\pi}\frac{Z_k Z_j}{r_{kj}}e^2 - \frac{1}{4\pi}\frac{\alpha_k Z_k{}^2 + \alpha_j Z_j{}^2}{2 r_{kj}{}^4}e^2 + \frac{A_{kj}(\sigma_k+\sigma_j)^{\eta_{kj}}}{r_{kj}{}^{\eta_{kj}}} - \frac{W_{kj}}{r_{kj}^6} \tag{3.11}$$

The first term is the Coulomb interaction between the ions of charge $Z_k e$ and $Z_j e$ (e is the absolute value of the electron charge). These charges are defined as the volume integral of electronic density in the volume of the ion. There are certain

arbitrarily in the definition of the ion volume, then Z_k is a parameter to fix and it could be fractional. The second term corresponds to the interaction charge-induced dipole, the parameter α is the electronic polarizability. Due to the low values of α this term can be neglected in certain cases. The stereometric repulsion (third term) is a classical analogous of the Pauli principle of exclusion, it states that two ions cannot indefinitely approach. This term added to obtain a repulsion effect. The last term is the van der Waals interaction and it is originated by the interaction dipole-dipole due the fluctuations of the atomic charge distribution.

The interaction charge-charge and charge-induced dipole are of long range. These kinds of interactions imply the use of expensive algorithms such as the Ewald sum technique or multipole expansion. Considering the electronic screening effect, we can assume that this interactions decay exponentially, so that the final form of our potential is

$$U(r_{kj}) = \frac{Z_k Z_j e^2}{4\pi r_{kj}} e^{\frac{-r_{kj}}{\lambda}} - \frac{(\alpha_k {Z_k}^2 + \alpha_j {Z_j}^2)e^2}{8\pi {r_{kj}}^4} e^{\frac{-r_{kj}}{\zeta}} + \frac{A_{kj}(\sigma_k+\sigma_j)^{\eta_{kj}}}{{r_{kj}}^{\eta_{kj}}} - \frac{W_{kj}}{r_{kj}^6} \qquad (3.12)$$

where λ and ζ are screening length. The parameters α and σ are reported in the literature. The others parameters are chosen so that the model reproduce the experimental values of the crystal structure, cohesive energy, bulk modulus and elastic constant c_{11}.

To attain better computational efficiency the interaction is truncated at a typical cutoff distance r_c. The discontinuity at r_c affects the energy conservation and the atomic motion, with atoms separated by a distance close to r_c. The potential function can be modified to eliminate the discontinuity both in itself and in its first derivative by replacing it with

$$\overline{U}(r) = \begin{cases} U(r) - U(r_c) - (r - r_c)\frac{dU(r_c)}{dr} & r \le r_c \\ 0 & r > r_c \end{cases}. \qquad (3.13)$$

3.3 Ensembles

Ensemble is a term from statistical mechanics; it means a statistical representative set of configurations. An ensemble can be defined as a whole collection of a very large number of systems in different possible microscopic states that the real system might be in, but all with common observed macroscopic attributes. For example,

each system of the canonical ensemble must have the same temperature T , volume V and number of particles N as the real system it represents.

Ensembles can be denoted and represented by different macroscopic properties, such as number of particles N, temperature T, pressure P, volume V, total energy E and chemical potential μ [17], etc. Each molecular dynamics simulation is performed under designated constraints of environment. In other words, the ensembles are specified in order to get the desired results. Thermodynamic ensembles can be defined according to different physical requirements [17, 25-28].

Canonical ensemble or NVT ensemble corresponds to a system with fixed volume V, number of particles N and temperature T, equilibrated with a heat bath with the same temperature. This ensemble will be used in situations where closed systems require no fluctuation of volume and also remain in a constant temperature.

Isothermal-isobaric ensemble or NPT ensemble represents a closed system with constant pressure P and temperature T. It is important for systems in a constant pressure situation. This ensemble is of great importance in equilibrating crystal-melt system at a constant low pressure and a constant melting point.

Microcanonical ensemble or NVE ensemble corresponds to a closed system with fixed volume V and total energy E. This ensemble is also significant because in molecular dynamics simulations, the stabilized volume and energy can greatly help to maintain a much stable equilibrium state in order to obtain more accurate data of thermodynamic properties.

Isoenthalpic-isobaric ensemble or NPH ensemble represents a closed system with fixed pressure P and enthalpy H. This ensemble can help to obtain the melting temperature at crystal-melt systems at a constant pressure.

Grand canonical ensemble or VTμ ensemble represents an open system, where the number of particles can change, with constant volume V, temperature T and chemical potential μ. This ensemble is not employed in our simulation because the whole process of our simulation is in a closed system.

3.4 Initial and boundary conditions

The simplest choice of initial position of atoms is to start with atoms at the sites of a regular lattice. The particle initial velocities are chosen at random direction,

usually following the Maxwell-Boltzmann distribution. Initial velocities are scaled so that the temperature is adjusted to a desire value. For certain numbers of time steps the velocity must be readjust to warrant that the total linear moment be null and the center of mass of the system stand at rest. The practice shows that the equilibrium is reached quite rapid, and there is no memory of the initial configuration, so that more careful attempts constructing a typical state are not very benefit.

The boundary conditions are chosen considering the characteristics of the system to be simulated. Finite and infinite systems are very different. In bulk system it is usual to use periodic boundaries condition to avoid the effect of surfaces. The idea of periodic boundaries is to surround the simulation box by virtual box which are made by replicating the main simulation box. There are to consequences of this periodicity. The first is that an atom that leaves the simulation box through a bounding face immediately reenters the box through the opposite face. The second is that the atom lying within a distance r_c of a boundary interact with atoms in an adjacent copy of the system, or, what is the same, with atoms near the opposite boundary (Figure 3.1) (this is called minimum image convection).

It is important to observe that even with periodic boundaries finite-size effects are present. How big the system has to be depends on the kind of system and the properties of interest. The only way to resolve this question is by a detailed numerical study. For free surfaces and subtracts it is necessary other kind of boundaries.

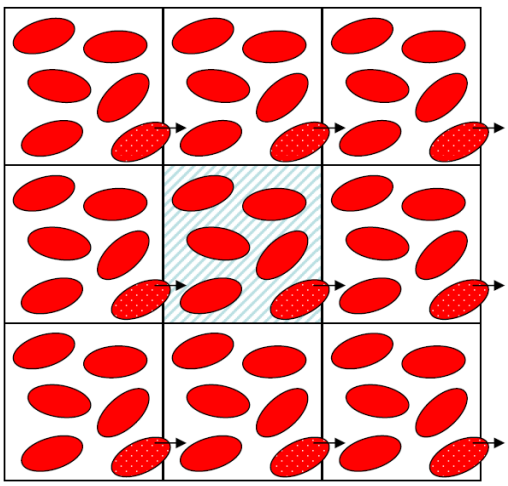

Figure 3.1 Scheme of periodic boundary conduction in two dimensions. Particles that leave the simulation box will be replaced by their images entering the box from the opposite side.

3.5 Radial distribution function

The radial distribution function or pair correlation function g(r) in a system of particles describes how the density of particles varies as a function of distance from a reference particle. When more than one chemical species are present the so-called partial radial distribution functions $g_{\alpha\beta}(r)$ may be computed as:

$$g_{\alpha\beta}(r) = \frac{V}{N^2}\langle \sum_{\alpha} \sum_{\beta} \delta(r - r_{\alpha\beta}) \rangle \quad (3.14)$$

where δ(r) is Dirac delta function, $r_{\alpha\beta}$ is the distance from a particle of the specie α to one of the specie β. The function g(r) is given by

$$g(r) = \sum_{\alpha} \sum_{\beta} c_{\alpha} c_{\beta} g_{\alpha\beta}(r) \quad (3.15)$$

where $c_{\alpha} = N_{\alpha}/N$ represents the concentration of atomic specie α. The radial distribution function is very important to characterize the structure and to detect structural changes.

The coordination number is the number of particles of the specie β inside a sphere of radius r with centre in a particle of the specie α:

$$n_{\alpha\beta}(r) = 4\pi\rho_{\beta} \int_0^r g_{\alpha\beta}(r) r^2 dr \quad (3.16)$$

where $\rho_{\beta} = N_{\beta}/V$ is density of the specie β in the sample.

The definition of g(r) implies that $4\pi\rho g(r)r^2dr$ is the mean number of atoms in a shell of radius r and thickness dr surrounding the atom. The radial distribution function is related to the experimentally measurable structure factor S(k) by Fourier transformation [17]:

$$S(k) = 1 + \rho \int_{-\infty}^{+\infty} (g(r) - 1) e^{-ik \cdot r} \, dr \quad (3.17)$$

The structure factor $S(k) = \langle \sum_{\alpha\beta} e^{-ik(r_{\alpha} - r_{\beta})} \rangle / N$ is a mathematical description of how a material scatters incident radiation. The structure factor is a particularly useful tool in the interpretation of interference patterns obtained in X-ray, electron and neutron diffraction experiments.

Chapter 4. Nonlinear time series analysis

Nonlinear time series analysis constitutes an important tool to study complex phenomena. The term nonlinear is used to distinguish these group techniques from classical linear time series analysis which are based in Fourier and correlation functions calculation, and which are not suitable in nonlinear dynamical systems. It must be mentioned that it is an active area of research; here we have limited to introduce some basic tools that we use later. It is presumed that the reader know the elementary concepts of chaotic dynamics. To whom is interested we recommend the book of Baker and Gollub [29] and the review of Eckmann and Ruelle [30].

4.1 Time series: reconstructing phase space

Chaotic time series are observed routinely in physics experiments. The analysis of chaotic time series has as objective to extract information of physical importance. This process can be divided in three steps:

1) separating the signal of physical interest from noise;
2) constructing an appropriate phase space in which the full structure of the strange attractor associated with the chaotic observation is unfolded;
3) evaluating invariant properties of the dynamics.

We will consider a single scalar observable measure at a fixed point. Let $s(t_0 + n\tau) = s(n)$ be the measured quantity, where t_0 is the initial time and τ is the sampling time. The quantity s(n) could be a voltage, the velocity of a fluid in a fixed point, or could be the temperature, etc.

The first task is to reconstruct the phase space of the system that generate the series s(n). But before it must be explained what means 'reconstruct the phase space'. We will consider as example a fluid that is described by Navier-Stokes partial differential equations. This system has infinite degrees of freedom that cannot be reestablished from s(n). But from a geometric point of view, and as this system is dissipative, the spatial pattern of the fluid can be described by an object of lower dimension than the original phase space. Then the idea is to model the evolution of the attractor itself and not the evolution in the full infinite phase space. In a nonlinear dissipative dynamical system different orbits converge to an attractor [31], the idea is to

reconstruct this low dimensional object (which does not depend of a particular initial condition) and to capture its main properties.

After transient has died out, the measurements s(n) provide the necessary information to reconstruct the finite dimensional space in which the system is evolving. In dynamical systems theory the concept of noise is associated with high dimensional dynamics, then reconstructing low dimensional object we are separating 'noise'. It must be mentioned that traditional techniques to diminish noise, such as signal filtering, could be dangerous and in some cases 'kill' useful information.

We will turn to the methods for reconstructing the phase space from the information on scalar measurements $s(n) = s(t_0 + n\tau)$. The principal idea is that the state of a system given by a set of variables, for example the position and the velocities of the particles of a system can be written as function of previous values of one of the variable of the system.

The dynamic of a system of dimension d defined by the generalized coordinates $x = [x_1, x_2, \dots, x_d]$ can be reconstructed using the lagged variables $s(n + T) = s(t_0 + (n + T)\tau)$, where T is an integer to be determined and the quantity s(n) could be any of the generalized coordinates x_i or a smooth function of the coordinates x_i. Then, using time lags variables we can create the desired d-dimensional vector:

$$y = [s(n), s(n + T), \dots, s(n + (d - 1)T)] \qquad (4.1)$$

The idea to use time-delays coordinates to reconstruct was introduced almost simultaneous by Packard *et al*. and Ruelle around 1980 [31].

Well, we now know how reconstruct the phase space from the scalar s(n), but, immediately arise the question: how must we choose the time delay T and the dimension d to construct the vector y? The answer to this question is a theorem [31], which states that it does not matter what time lag one chooses while the dimension d be chosen is larger than $2d_A$, where d_A is the dimension of the attractor. The procedure of choosing sufficient large d is formally known as embedding, and any dimension that works is called an embedding dimension d_E. Once one has achieved a large enough $d = d_E$, then any $d \geq d_E$ will also provide an embedding.

4.2 Choosing time delays

According to the embedding theorem any time lag will be acceptable, but this is not very useful to extract the physics from the time series. If we choose T too small, then the coordinates s(n + jT) and s(n + (j + 1)T) will be so close to each other, then such coordinates are not independent. Similarly, if T is too large, then s(n + jT) and s(n + (j + 1)T) are completely independent of each other in a statistical sense and the orbits are projected onto two totally unrelated directions.

As a first approach, we can consider s(n) as random numbers that follow certain unknown distribution. Then, the time lag can be taken as time for which the linear autocorrelation function first vanishes:

$$C_L(t) = \frac{\frac{1}{N}\sum_{m=1}^{N}[s(m+t)-\bar{s}][s(m)-\bar{s}]}{\frac{1}{N}\sum_{m=1}^{N}[s(m)-\bar{s}]^2} \tag{4.2}$$

$$\bar{s} = \frac{1}{N}\sum_{m=1}^{N} s(m) \tag{4.3}$$

This independence is only in the linear fashion [31].

In information theory the average mutual information is in certain way a generalization of linear autocorrelation. Let $P_A(a_i)$ be the probability to find the system A in the state a_i, similarly $P_B(b_k)$ is the probability of occurrence of b_k in B, and $P_{AB}(a_i, b_k)$ is the joint probability of occurrence a_i and b_k. The average mutual information is defined as

$$I_{AB}(T) = \sum_{a_i,b_k} P_{AB}(a_i, b_k)\log_2 \left[\frac{P_{AB}(a_i,b_k)}{P_A(a_i)P_B(b_k)}\right] \tag{4.4}$$

Note that when the measurements of A and B are completely independents, $P_{AB}(a_i, b_k)=P_A(a_i)P_B(b_k)$ and $I_{AB}(T) = 0$.

In terms of the time series s(n), the average mutual information between observations at n and n + T, is the average amount of information about s(n + T) we have when we make an observation of s(n):

$$I(T) = \sum_n P(s(n), s(n+T))\log_2 \left[\frac{P(s(n),s(n+T))}{P(s(n))P(s(n+T))}\right] \tag{4.5}$$

As a prescription, we choose the time lag T where the first minimum of I(T) occurs. If the average mutual information has no minimum, without much grounds beyond intuition, we take T such that $I(T)/I(0) \cong \frac{1}{5}$, or simple it set T = 1 or 2.

4.3 Choosing the embedding dimension

If the attractor is properly unfolded by choosing a large enough d_E, then any property associated with the attractor which depends on distance between points in phase space should become independent of the value of the embedding dimension once the necessary d_E has been reached. After that, increasing d_E should not affect the value of these properties, and, in principle, the appropriate necessary embedding dimension d_N can be established by computing such a properties for increasing values of d_E until variation with d_E ceases.

Other important method to determine d_N is the false nearest neighbors. The idea is that the necessary embedding dimension is that for which false neighbors are eliminate. False neighbors are those that arose by virtue of having projected the attractor into too low dimensional space.

In a dimension d each vector $y = [s(n), \dots, s(n + (d - 1)T)]$ has a nearest neighbor y^{NN}. The Euclidian distance in dimension d between y and y^{NN} is

$$R_d^2 = [s(n) - s^{NN}(n)]^2 + \cdots + [s(n + (d - 1)T) - s^{NN}(n + (d - 1)T)]^2 \quad (4.6)$$

In dimension d + 1, the distance is given by

$$R_{d+1}^2 = R_d^2 + [s(n + dT) - s^{NN}(n + dT)]^2 \quad (4.7)$$

If R_{d+1} is large, we can presume it is because the near neighborliness is due to the projection from some higher-dimensional attractor down to dimension d. By going from dimension d to dimension d + 1, we have unprojected these two points away from each other. Some threshold size R_T is required to decide when neighbors are false. Then if

$$\frac{|s(n+dT) - s^{NN}(n+dT)|}{R_d} > R_T \quad (4.8)$$

the nearest neighbors are false. In practice, for values of R_T in the range $10 \leq R_T \leq 50$ the number of false neighbors identified by this criterion is constant.

The fact that points are nearest neighbors does not mean they are close on a distance scale set by the approximate size R_A of the attractor. If the nearest neighbor to y is not close, so $R_d \approx R_A$, then the distance R_{d+1} will be about $2R_d$. This means that distant, but nearest neighbors will be stretched to the extremities of the attractor when they are unfolded each other, if they are false nearest neighbors.

As a second criterion of falseness of nearest neighbors we have

$$\frac{R_{d+1}}{R_A} \geq 2 \tag{4.9}$$

As a measure of R_A one may use the quadratic mean value of the observation

$$R_A^2 = \frac{1}{N}\sum_{k=1}^{N}[s(k) - \bar{s}]^2 \tag{4.10}$$

When nearest neighbors falling either in one of these two criteria they are declared false. If the signal is corrupted by noise or other high dimensional signal, and the level of contamination is low, the residual percentage of false neighbors gives an indication of the noise level.

4.4 Invariant of the dynamics: dimension

Attractor dimension are the most intensely studied invariant quantity for dynamical systems. Such interest is motivated by the fact that chaotic attractor have fractional dimension [30, 31], in contrast with regular systems which have integer dimension. Currently the calculus of dimension is used to demonstrate the existence of chaos.

The concept of dimension (D) can be defined through the relation

$$V \propto L^D \tag{4.11}$$

where V is the (hyper) volume and L is a characteristic length parameter. For an objects in the plane, we can calculate its area decomposing it into n small squares of side length L, the area will be nL^2 in the limit $L \to 0$. For a body in real space its volume will be nL^3 as $L \to 0$, and so on. Then, a general definition of dimension could be

$$D = \lim_{L\to 0} \frac{\log V}{\log L} \tag{4.12}$$

In general we have a set of point of the attractor. Then dividing the space in cubes of side length L and counting the boxes that at least contain one point we can calculate the dimension. Repeating this procedure for several orders of magnitude of L we can calculate the tendency of D. It is obvious that the largest value of D calculable is the embedding dimension. If the embedding dimension is not large enough to unfold the attractor it is expected that the attractor's projection fills the space, resulting in an estimated dimension equal to the embedding dimension. As the embedding dimension increases through the minimum required for complete unfolding the attractor, the calculate dimension 'saturate', it turned independent of the embedding dimension.

Still more general than the above definition is the concept of generalized dimension. The generalize dimension is defined as

$$D_q = \lim_{r\to 0} \frac{1}{q-1} \frac{\log \sum_{i=1}^{N} p_i^q}{\log r} \tag{4.13}$$

where the d-dimensional phase space has been partitioned into boxes of size r^d; p_i is the probability that the trajectory x visits box i and N is the number of non-empty boxes. The generalized dimension provides a whole spectrum of invariant quantities for $-\infty < q < \infty$. For q = 0, the sum reduces to the number of non-empty boxes. The D_0 is called the topological or fractal dimension. For q = 1, the D_1 is called the information dimension. The D_2 is called correlation dimension.

The numerator of the correlation dimension

$$D_2 = \lim_{r\to 0} \frac{-\log \sum p_i^2}{\log r} \tag{4.14}$$

is a measuring of the probability of finding a pair of random points within a given partition element. A simple and computational efficient means of estimating $\sum p_i^2$ is counting how many pairs of points have a separation distance less than some value r [32, 33]:

$$C_2(r) = \frac{2}{N(N-1)} \sum_{i\neq j} \theta(r - |x(j) - x(i)|) \tag{4.15}$$

The correlation dimension is the slope of the curve $\log C_2(r)$ versus $\log r$. In standard practice several curves $\log C_2(r)$ versus $\log r$ are plotted for increasing values of embedding dimension. For embedding dimensions smaller than the minimum required for complete unfolding of the attractor, the slope of the plot will equal the embedding dimension. As the embedding dimension increases, the slope of $\log C_2(r)$ versus $\log r$ plot should saturate at a value equal to the attractor's dimension.

Theoretically, the dimension D_2 is the slope of the $\log C_2(r)$ versus $\log r$ plot in the $r \to 0$ limit, but this region of the plot is dominated by noise. Therefore it is necessary to identify a scaling region at intermediate length scales, where a constant slope allows reliable estimation of the dimension.

4.5 The Lorenz chaotic model

The Lorenz equations [31] are derived from a finite mode truncation of the partial differential equation describing the thermal convection in the lower atmosphere:

$$\dot{x} = \sigma(y - x) \tag{4.16}$$

$$\dot{y} = -xz + rx - y \tag{4.17}$$

$$\dot{z} = xy - bz \tag{4.18}$$

Many authors have adopted the Lorenz equations as a model of low dimensional chaotic behavior.

As the parameter r, representing the ratio forcing to damping, is increasing the system undergoes a sequence of transitions from regular to more complex. Figure 4.1 shows a typical chaotic time series. As illustration of the method of dynamic reconstruction we used time series of this system. First, it was calculated the average mutual information (Figure 4.2) and the percentage of false nearest neighbors (Figure 4.3). Following the above discussion, we take as time lag the value for which the mutual information has its first minimum, $T = 11$. And from the graphic of false nearest neighbors it is seen that the required embedding dimension is 3, in agreement with our model.

Figure 4.4 shows the reconstructed attractor. In Figure 4.5 is the attractor obtained from the numerical integration of equations (4.16)-(4.18). In spite the reconstructed attractor appears with the borders folded, these result is fascinating. In Figure 4.6 is shown the correlation function C_2 versus r in logarithm scales. From this we find that the fractal dimension is approximately $D_2 = 2.07$.

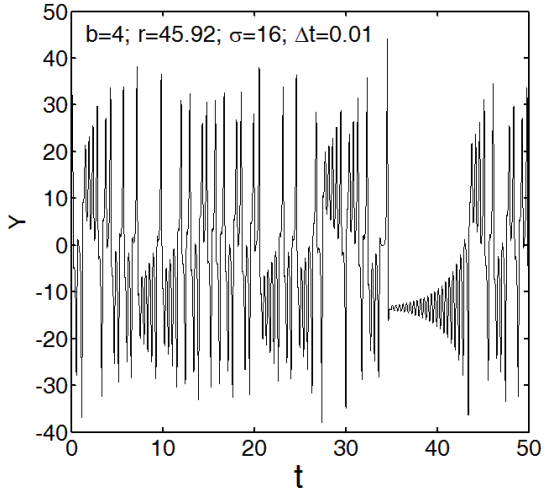

Figure 4.1 Chaotic time series y(t) of Lorenz model.

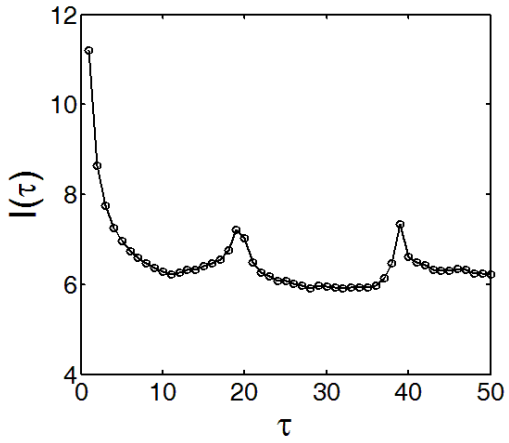

Figure 4.2 Average mutual information for Lorenz data.

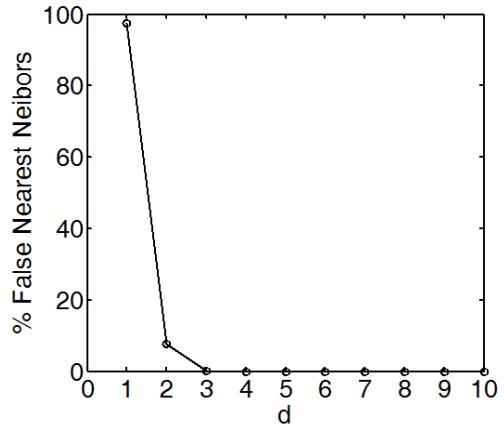

Figure 4.3 Percentage of false nearest neighbors as function of embedding dimension for Lorenz model.

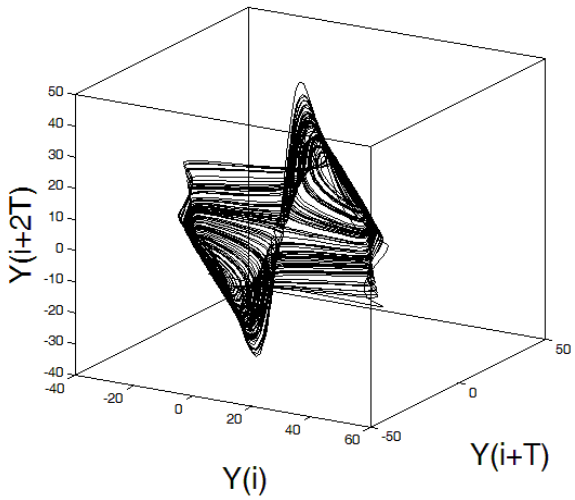

Figure 4.4 Reconstructed Lorenz attractor using time-delay coordinates.

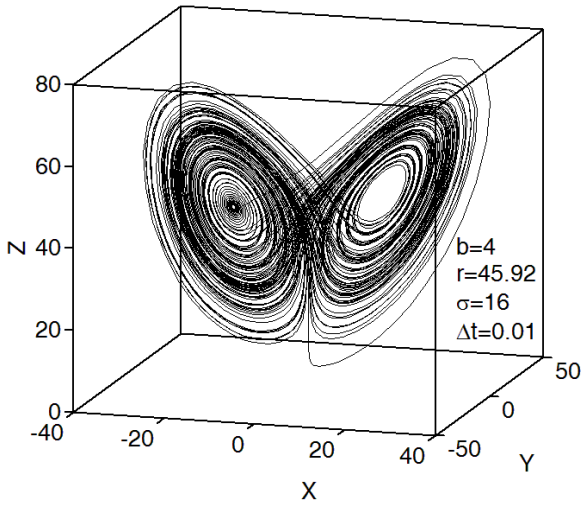

Figure 4.5 Lorenz attractor.

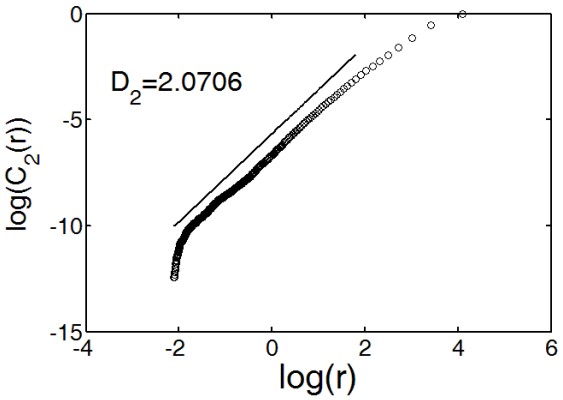

Figure 4.6 Correlation function $C_2(r)$ for Lorenz data ($C_2(r) \sim r^{D_2}$).

Chapter 5. Anomalous behavior of $CaTiO_3$ around 200 K

This chapter is devoted to the study of low temperature elastic behavior of the $CaTiO_3$. The elastic behavior is studied experimentally by pulse-echo ultrasonic techniques in the range the temperature from 300 to 20 K. Using molecular dynamic simulations we make a comparative study of the elastic response of a mono-domain and a poly-domain configurations. This comparatives study allows analyzing the effect domain wall motion and defects in the response of this system. The dynamics of the mono and poly-domain are studied through nonlinear time series analysis.

5.1 Experimental results

A polycrystalline sample of $CaTiO_3$ was obtained by standard ceramic method. The ultrasound attenuation and velocity were simultaneously measured by the conventional pulse-echo method [34, 35]. This method allows small variations in the phase velocity to be measured with great accuracy by determining the ultrasound wave traveling time in a round trip.

A polycrystalline ceramic sample can be considered as an isotropic elastic medium. In this approximation, Young's modulus E, shear modulus G, bulk modulus B and Poisson's ratio σ are given by [36]:

$$E = \frac{\rho v_t^2 (3v_l^2 - 4v_t^2)}{v_l^2 - v_t^2} \tag{5.1}$$

$$G = \rho v_t^2 \tag{5.2}$$

$$B = \rho \left(v_l^2 - \frac{4}{3} v_t^2\right) \tag{5.3}$$

$$\sigma = \frac{v_l^2 - 2v_t^2}{2(v_l^2 - v_t^2)} \tag{5.4}$$

where v_l and v_t are the longitudinal and transverse sound velocities.

Longitudinal and transverse ultrasound velocity and attenuation versus temperature are shown in Figure 5.1. In the velocity versus temperature curves, an anomaly around 200 K can be identified. In the same range of temperatures there is an attenuation peak, indicating the presence of poorly characterized strains.

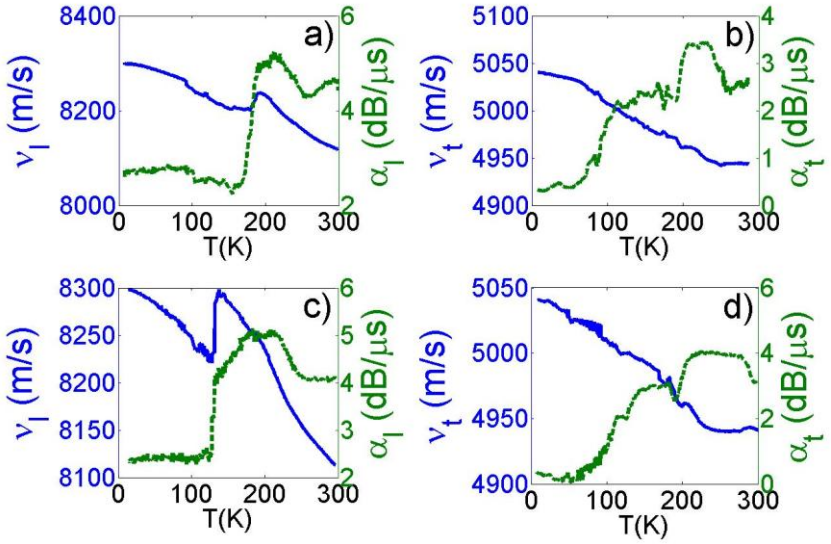

Figure 5.1 Sound velocity (solid line) and attenuation coefficient (dashed line) versus temperature. Items (a) and (b) are for heating process, (c) and (d) for cooling.

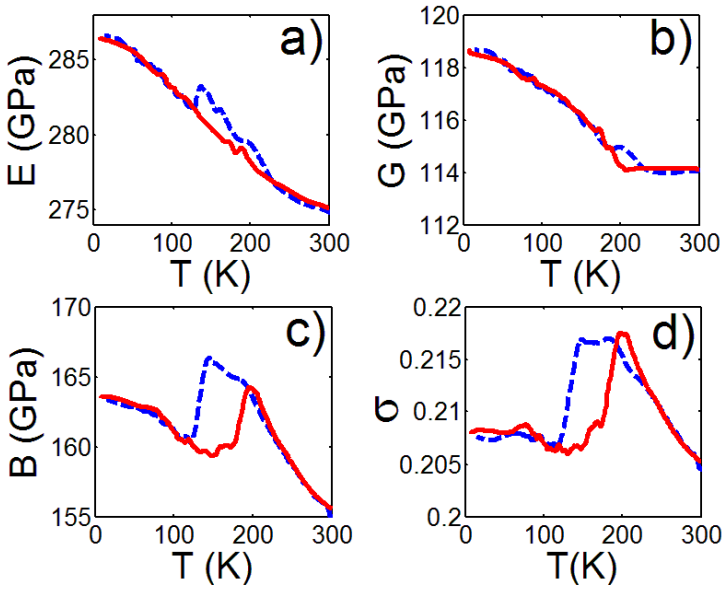

Figure 5.2 Elastic moduli versus temperature (experimental measurements): a) Young modulus, b) shear modulus, c) bulk modulus and d) Poisson ratio. Cooling curves: dashed; heating curve: solid.

The temperature dependence of the Young's modulus, shear modulus, bulk modulus and Poisson's ratio measured at 10 MHz are shown in Figure 5.2. There is a hardening in Young's modulus and bulk modulus at approximately 200 K. Correspondingly, Poisson's ratio rises to a maximum around 200 K with decreasing temperature, followed by a fall at lower temperatures.

Although this ultrasonic technique is very sensitive in revealing subtle structural phase transitions, the presence of ultrasonic attenuation peaks sometimes occurs due to dynamical reasons that do not involve phase transitions. Similar anomalies were reported in $SrTiO_3$ by Scott and Ledbetter [37], which were explained as purely dynamical phenomena. The anomalous ultrasonic behavior in both longitudinal and transversal modes could be attributed to the occurrence of ferroelastic domains and domain walls motion. Complementary information about domain walls motion could be obtained at lower measuring frequencies using the method of dynamic mechanical analysis [38-41].

5.2 Simulation of a mono–domain configuration

Molecular dynamics simulations of $CaTiO_3$ were performed with a two-body central force based on the Vashishta-Rahman interatomic potential:

$$U_{ij}(r) = \frac{Z_i Z_j}{r} e^{-\frac{r}{\lambda}} + \frac{H_{ij}}{r^{\eta_{ij}}} - \frac{D_{ij}}{2r^4} e^{-\frac{r}{\xi}} - \frac{W_{ij}}{r^6} \qquad (5.5)$$

where the first term represents the Coulomb interaction between two ions of effective charges Z_i and Z_j (in units of electron charge e) at the interatomic distance $r \equiv |r_i - r_j|$. The second term represents the steric effects, in which H_{ij} and η_{ij} are the strength and exponent of steric repulsion, respectively. The third term represents the charge-induced dipole interaction, due to the electronic polarizabilities of atoms, where D_{ij} is the strength of the charge-dipole attraction, and the last term is the induced dipole-dipole potential, where W_{ij} is its strength. Parameters λ and ξ are the screening length for Coulomb and charge-dipole terms, respectively. The interaction potential is truncated at the cutoff radius r_c.

Parameters in the potential were determined by fitting the model to some selected physical properties: cohesive energy, bulk modulus, elastic constants and lattice parameters for the orthorhombic structure. Thus the following were set: $Z_{Ca} = 0.9697$, $Z_{Ti} = 1.9394$, $Z_O = -0.9697$, $\lambda = 5.5$ Å, $\xi = 3.25$ Å and cutoff radius $r_c = 8.0$ Å. Other parameters are summarized in Table I.

Table I. Parameter set for two-body Vashishta-Rahman potential.

Parameter	Ca-Ca	Ca-Ti	Ca-O	Ti-Ti	Ti-O	O-O
η_{ij}	11	9	9	11	9	7
$H_{ij}(eV\ Å^{\eta})$	8283.57981	216.64756	2365.84091	25.22251	374.99707	684.09897
$D_{ij}\ (e^2\ Å^3)$	2.0687	1.0343	2.1627	0	1.1284	2.2568
$W_{ij}\ (eV\ Å^6)$	0	0	242.6390	0	0	0

All the molecular dynamics simulations were performed with LAMMPS [42] using the NPT and NVT ensembles, with a time step $\Delta t = 2$ fs. A perfect mono-crystal configuration comprising $8 \times 8 \times 40$ unit cells (N = 51200 particles) was built in a simulation box with periodic boundary conditions in all directions, Figure 5.3. Coordinates of atoms in the orthorhombic-Pbnm unit cell were taken from data reported in Ref. [43]. The system was thermalized in the NPT ensemble, leaving it to evolve for 20,000Δt at 300K. The calculations were performed in 3 computers of 6 cores Phenom II X6 1100T (3.2 GHz and 16 Gb). For each temperature the running time was around of half hour. At 300 K, the density was $\rho = 4.0274\ g/cm^3$, very close to the reported experimental value $\rho = 4.0437\ g/cm^3$ [43].

From the equilibrium configuration, the system was cooled from 300K to 20K, thermalizing after each 10 K step for 5000Δt . At each temperature, the system was deformed uniformly, each 500Δt for 10 000Δt, up to 1.001 times the initial equilibrium volume in the NVT ensemble. Later, the same process was repeated to obtain a deformation of 0.998 times the initial equilibrium volume. The deformations were small enough to keep the system in the linear response regime.

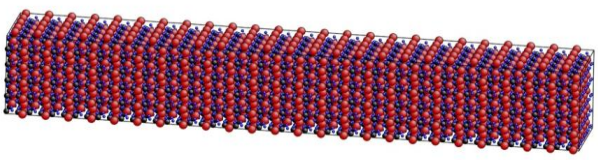

Figure 5.3 Mono-domain of $CaTiO_3$ at 300K.

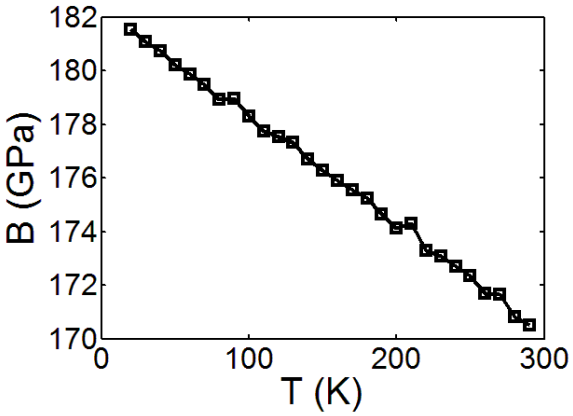

Figure 5.4 Molecular dynamics simulation of bulk modulus for a mono-domain of $CaTiO_3$.

The simulated bulk modulus was determined from the standard definition [44]:

$$B = -V_0 \frac{dp}{dV} \tag{5.6}$$

The bulk modulus decreases with increasing temperature almost linearly (see Figure 5.4). Very small departures from linear dependence are observed at 90 and 210 K. Simulations were repeated for different initial configurations and always were observed the same two peaks. This observation was reproduced in systems with the same number of particles but with different simulation box geometries. The magnitude of the bulk modulus is higher than that observed experimentally. This can be explained by the fact that simulations were performed on an ideal crystal without interstices and other defects.

5.3 Simulation of a poly–domain configuration

The crystal structures are often corrupted by defects such as grain boundaries, twins and dislocations. However, simulations are limited to the box geometry. Then, surface effects as well as the effects of grain boundaries are eliminated by the periodic boundary conditions. In spite of these limitations, it is possible to simulate a poly-domain structure with the typical defects such as twins and dislocations.

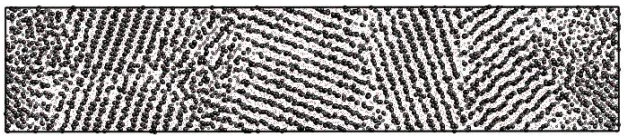

Figure 5.5 Poly-domain structure of $CaTiO_3$ at 300K.

A new simulation box was employed consisting of 8 × 8 × 40 ideal $CaTiO_3$ cubic cells (N = 12800 particles), with a lattice parameter a = 3.8967 Å. The temperature was fixed at 3600 K in the NPT ensemble for 50,000 Δt, during which the system completely melted. After this, the system was cooled from 3600 to 300 K at a rate of 0.5K/ps.

At 300 K the mean density was ρ = 3.6542 g/cm^3, lower than that of the mono-domain structure. The polycrystalline structure and defects like interstices could be detected by simple inspection, as are shown in Figure 5.5. The crystal domains are well defined with wall width of the order of the unit cell parameters. As for the mono-domain, the system was cooled from 300 to 20 K, thermalizing at each 10 K for 5000Δt.

At each temperature, the system was deformed uniformly, each 500Δt for 10,000Δt, up to 1.001 times the initial equilibrium volume in the NVT ensemble. Later, the same process was repeated to obtain a deformation of 0.998 times the initial equilibrium volume.

All the deformations were performed in the linear response region. For the poly-domain configuration the fluctuations are considerably larger than in the mono-domain (compare Figures 5.4 and 5.6a), so the simulations were repeated 40 times under different initial conditions and results were averaged to smooth the curve, Figure 5.6b. The bulk modulus is 60 % lower than in the mono-domain, while the volume increases only in 10 %. Such smooth in the bulk modulus is due, partially, to the occurrence of interstices.

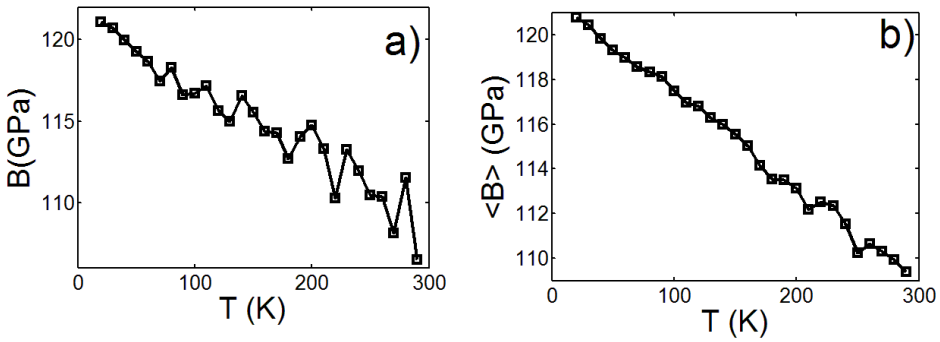

Figure 5.6 Molecular dynamics simulation of bulk modulus for the poly-domain configuration: a) single curve and b) average of 40 curves for different initial conditions.

Around 210 K it can be observed an increment in bulk modulus. Although the increment bulk modulus is modest, is meritorious that this occurs in the same temperature range as in experiment. The greater values on experiment can be explained by effect of other factors as grain texture, obviously not considered in the simulation.

The $g_{\alpha\beta}(r)$ were calculated at various temperatures, in order to look for possible structural modifications. No change in symmetry was detected in the analysis of partial and total pair correlation functions in the range from 20 to 300 K. Additionally, the total pair correlation function was calculated at 210K for a region inside a domain and a region comprising twin walls, Figure 5.7 . No significant structural changes between bulk and interfaces could be found. The pair correlation function calculated inside the crystallite coincided with that calculated for the mono-domain [24].

The perovskite phase transition involves small atomic displacements. Transitions from orthorhombic to tetragonal, and then to cubic occur through tilting of the TiO_6 octahedra [45], thus no significant displacement occurs. Structural changes can be also observed through bond angle distributions. Ti-Ti-O bond angle distribution was calculated from the average positions of atoms in the mono-domain and poly-domain, as shown in Figure 5.8. The bond angle distribution remains practically unchanged from 20 to 300 K, reinforcing the idea that no phase transition occurs at this range of temperature.

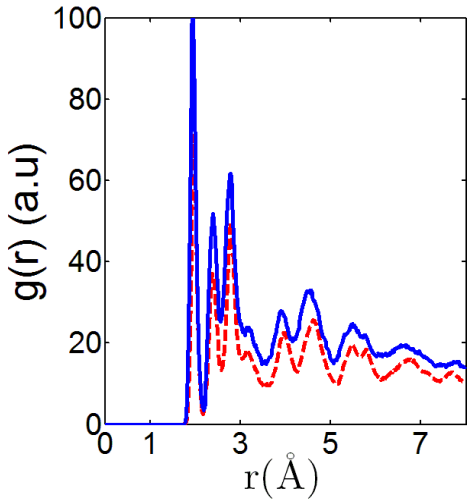

Figure 5.7 Pair correlation function at 210 K calculated inside a domain (solid line) and across domain walls (dashed line).

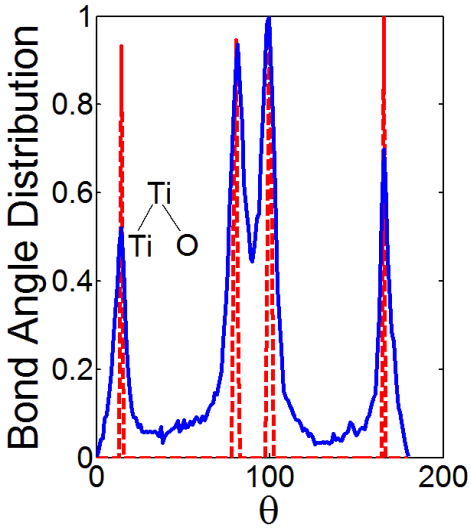

Figure 5.8 Ti-Ti-O angle distribution for a mono-domain (dashed line) and a poly-domain (solid line) at 210 K.

If phase transitions are absent, then no abrupt change in the average macroscopic variables or their derivatives with respect to temperature will take place. Nevertheless, a change in the dynamics must affect to a certain extent the evolution of macroscopic variables over time. The time average total energy ($\overline{E}$) was calculated during 10,000 Δt for the mono-domain and poly-domain in the interval from 20 to 300 K in the NVT ensemble, Figure 5.9. In this interval of temperatures, $\overline{E}$ increases linearly with the increasing temperature, in agreement with the classical nature of the simulations. The continuous and linear rise of $\overline{E}$ with temperature is another sign that no phase transition occurs.

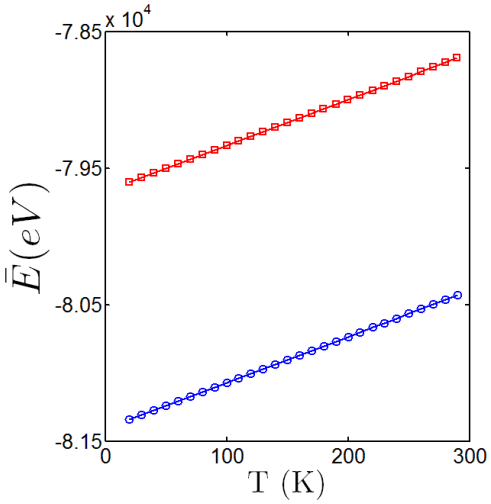

Figure 5.9 Average total energy versus temperature for a monodo-main (circles) and a poly-domain (squares) of $CaTiO_3$.

A possible explanation of the anomalies observed could be related with the occurrence of avalanches in domain walls. Accumulated stress in domain wall relaxes in form of avalanches that are transmitting through neighbors domains. Experimentally the occurrence of avalanches in domain wall have been observed through calorimetric (heat flux) and acoustic emission [14]. Avalanches are self critically organized phenomena and the frequency of occurrence is given by a power law [46].

The occurrence of avalanches must be reflected as fluctuations in macroscopic variables. As macroscopic observable we choose the pressure P in the NVT –ensemble. Pressure was measured 810 000 times each 2 fs and the occurrence probability density function f(P) was constructed, been f(P)dP the probability to have fluctuation with intensity between P and P + dP . Figure 5.10 shows f(P) for the mono-domain and poly-domain at several temperatures in double logarithmic scales. Fluctuations are stronger in the poly-domain, which also can be direct observed in bulk modulus. For highs values of P the curves can be approximated by straight lines, e.g., the density of probability follows a power law $f(P) \sim P^{-\alpha}$ with $\alpha \cong 8.2 \pm 0.1$. By appropriate shifting the curves can be brought to cover each other (Figure 5.10).

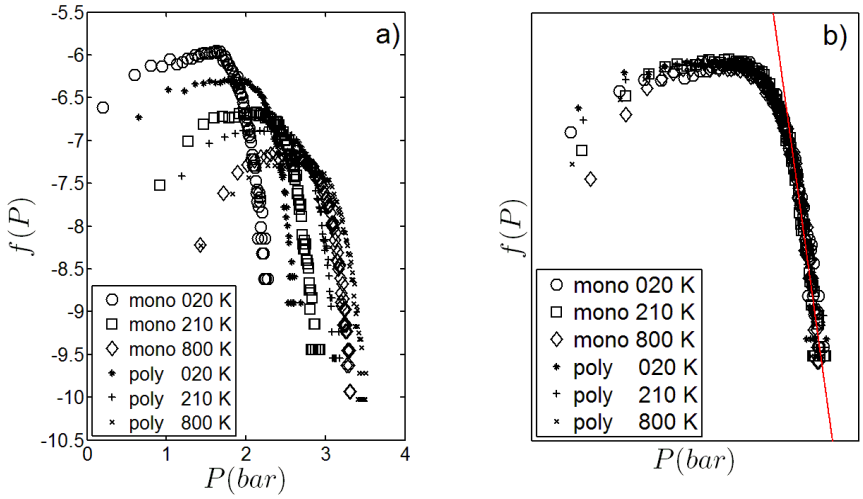

Figure 5.10 Distribution function of fluctuation peaks for mono-domain and poly-domain configurations in log-log scales. a) Bigger fluctuations follow a power law, b) using appropriate coordinate scaling all curves overlap.

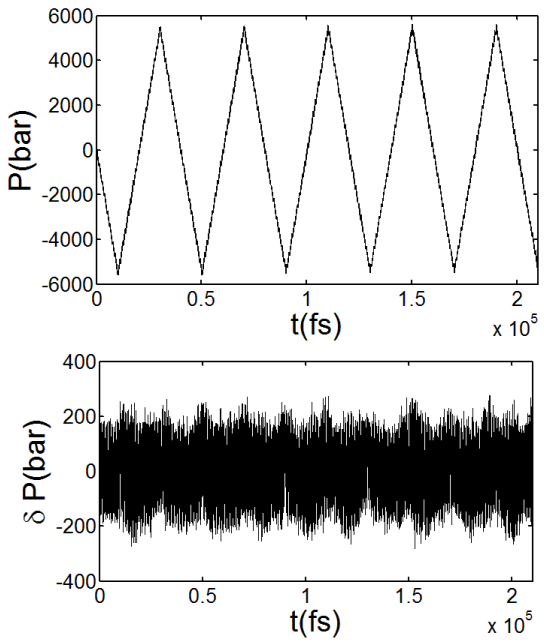

Figure 5.11 a) Temporal evolution of pressure under alternates volumetric deformation. b) Fluctuations are projected in horizontal axis after removing smooth component.

Although this result is very interesting it does not allow a definitive conclusion to be reached about the existence or otherwise of avalanches, because the same behavior is observed in the mono-domain and poly-domain. Fluctuations where analyzed also under a constant deformation, Figure 5.11. Again power law was found for f(P) with the same exponent α for both systems.

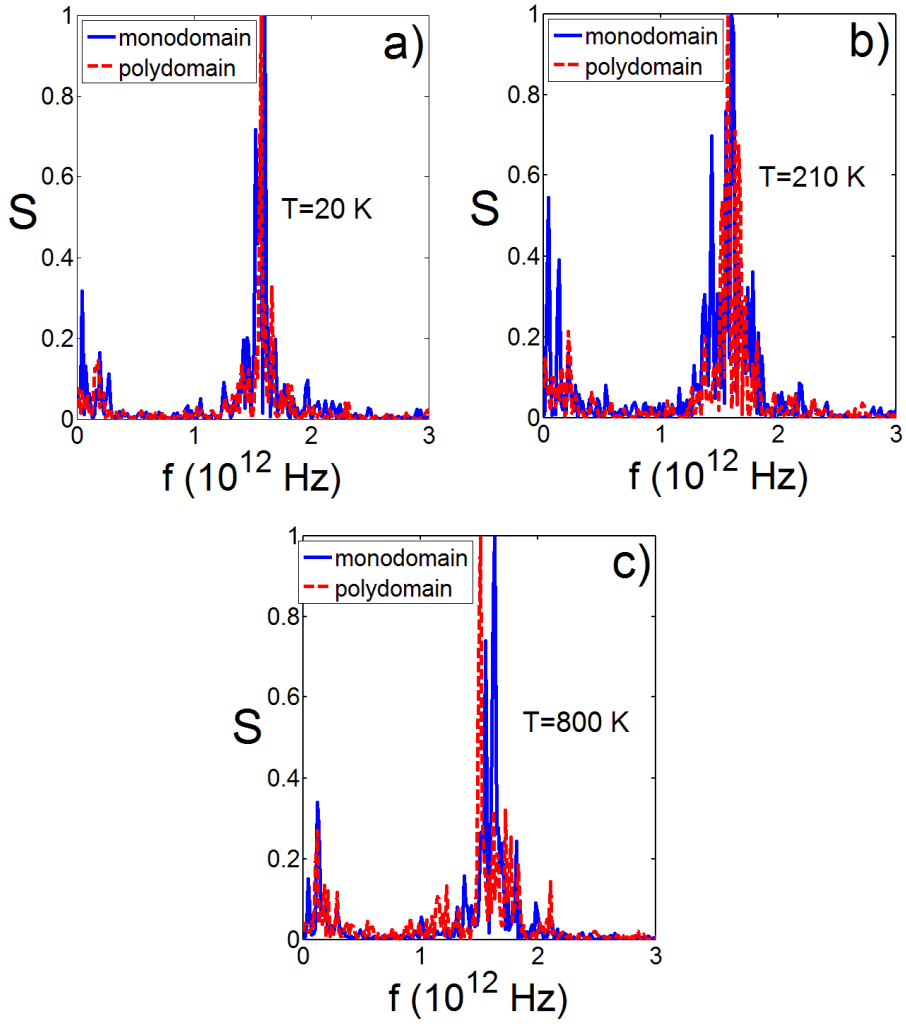

Figure 5.12 Power spectrum of fluctuations of energy for a mono-domain (dashed line) and a poly-domain (solid line). Each curve is normalized with respect to its highest peak.

5.4 Time series analysis

The power spectra (S) of the energy fluctuations $E(t) - \overline{E}$ were calculated for different temperatures, as shown in Figure 5.12. There are clear differences between the power spectrum pattern of the temporal series generated at 210 K and the spectra obtained for 20 K and 800 K. With the increase in the temperature the fluctuations increase. At low temperatures there is only one main peak in the power spectrum of the poly-domain. At 210 K, there are three main peaks. At the higher temperature, only one main peak appears again. For the mono-domain, there is an increase in the complexity of the power spectrum at 210 K. This behavior is more marked in the poly-domain.

The power spectrum of energy time series gives an idea about the dynamical differences between both systems. Due to the nonlinear nature of the interaction the Fourier transform of time series is not enough to characterize the dynamics of this system. In principle, the dynamic of the system can be characterized in phase space. Using coordinates and velocities of particles is possible to calculate parameters like Liapunov exponents and Kolmogorov-Sinai entropy; which allow detecting the changes in the dynamics [47, 48]. But for our system such approach implies serious difficulties due the large number of particles. Then, dynamic reconstruction and characterization from time series approach is more preferable.

Phase space is reconstructed using time delay coordinates [30, 31, 49]. Let $\{s_i\}$ be the time series, in our case it is the hydrostatic pressure measurements each Δt = 2 ps. Delay coordinates are defined as the set of values $[s_i, s_{i+\tau}, \dots, s_{i+(d-1)\tau}]$, being τ and d integers. τ is the time lag and d is the dimension of the space. d must be sufficient large to correctly describe the reconstructed dynamics.

Time lag is chosen by means of the average mutual information [31],

$$I(\tau) = \sum_{i=1}^{N} P(s_i, s_{i+\tau}) \log_2 \left[\frac{P(s_i, s_{i+\tau})}{P(s_i)P(s_{i+\tau})}\right]$$

As thumb rule, τ is taken as the first minimum of $I(\tau)$ [31]. Figure 5.13 shows the mutual information calculated from the times series for mono-domain and poly-domain configurations. It is surprising the behavior of poly-domain system which corresponds with the dynamic of discrete system, i.e., a map. The minimum value fluctuates between 6 and 10 in the temperature range from 20 to 300 K. All the subsequent calculations were performed for time delays of 6 and 10, resulting in all the case in the same results.

The embedding dimension is determined by the method of false neighbors. Figure 5.14 shows the behavior of false nearest neighbors calculated from time series of 20000 points. In the case of poly-domain it is zero for d = 22 at 210 K, while for the mono-domain false nearest neighbors never is zero. Such behavior indicates that in the poly-domain exists a well defined low dimension dynamics in addition to stochastic high dimensional proper of the system. This can be interpreted as result of domain wall motion. Domain wall motion is a kind of collective motion in which a group of atom moves as a whole then their dynamics can be described by few degrees of freedom.

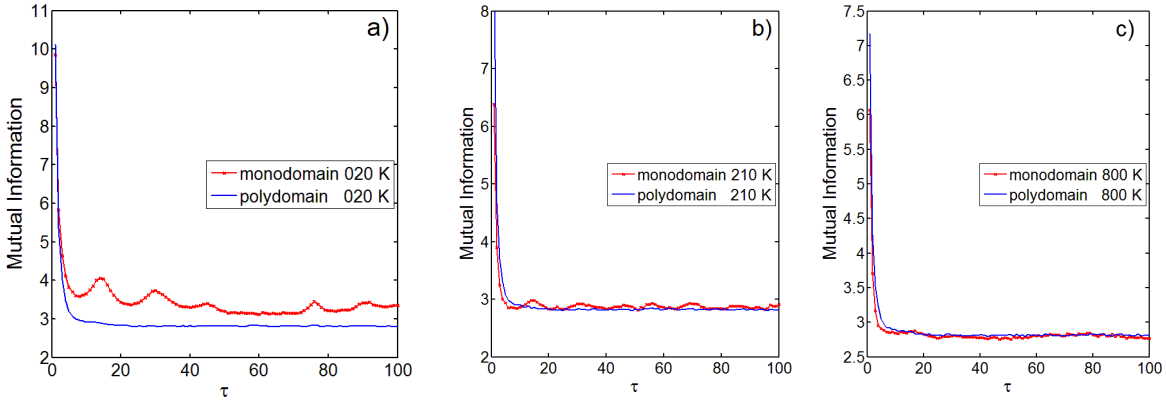

Figure 5.13 Mutual information determined from time series of 105 000 points.

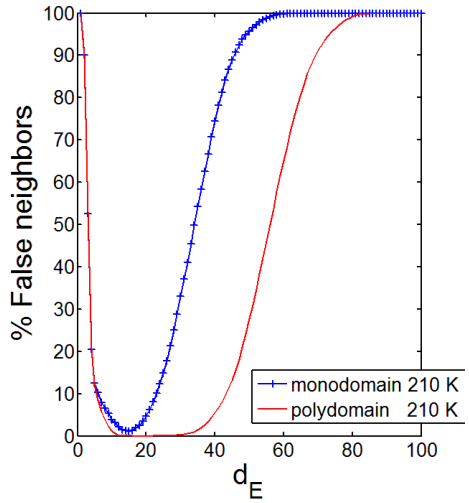

Figure 5.14 Determining the embedding dimension by false neighbors' method, 20 000 point were used with time lag T = 10.

In principle it is possible to characterize low dimensional dynamics knowing the time delay and embedding dimension. A straight way is through correlation dimension d_c, a fractal dimension. It is estimated by the algorithm of Grassberger-Procaccia [32, 33]. The method is based in the determination of correlation integral C(r), which for $r \to 0$ behalves as $C(r) \sim r^{-d_C}$.

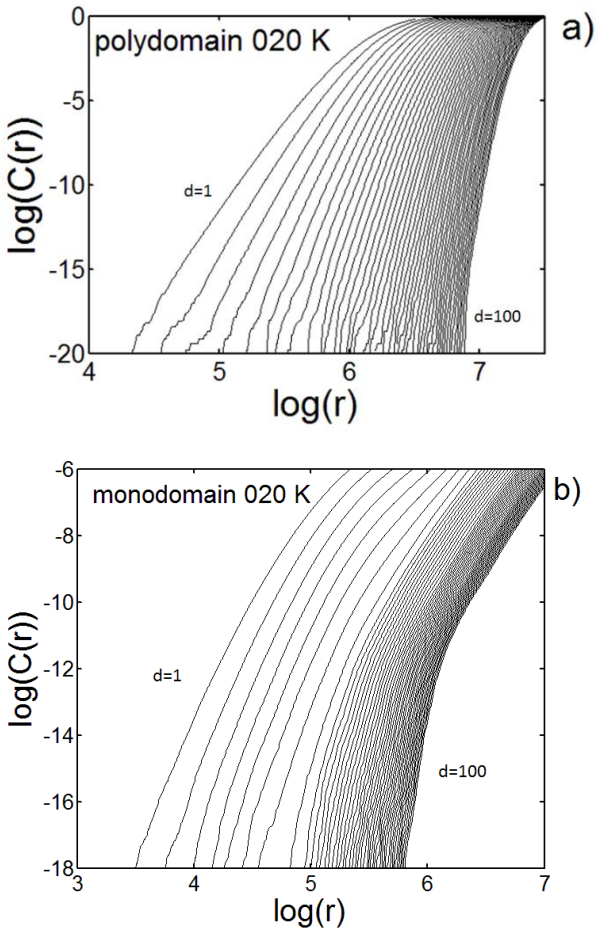

Figure 5.15 Correlation integral versus distance in logarithm scales at 20 K, d_E = 10, 12, 14,..,100. a) mono-domain and b) poly-domain.

Figure 5.15 display C versus r in a log-log plot. For the mono-domain there are two scaling regions, e.g. there are two windows in which the curve are straight lines. As d_E increases the exponent γ increases and it must reach a plateau at d_E equal to the lower integer bigger or equal to d_C [31], but when noise is sufficient strong this occurs for higher values of d_E and the correlation dimension is in general overestimated [31].

Around 210 K the curves C(r) have only one scaling region. The γ versus d_E plot has very short plateau for the poly-domain at $d_E = 54$ (see Figure 5.16) from which it is approximately estimated $\gamma \cong 26.34$. Then around this temperature a new mode is activated, probably associated with domain wall motion.

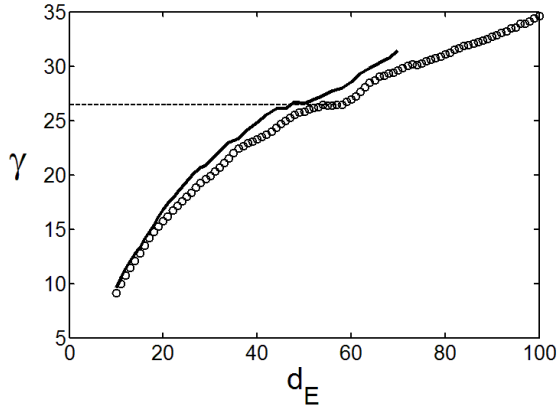

Figure 5.16 γ versus d_E for the mono-domain (solid line) and poly-domain (circles).

There are two important conclusions derived from the study of the dynamics of these systems. In one hand, the differences between mono-domain and poly-domain persist in all range of temperatures, which was also confirmed by other properties such as the bulk modulus, the distribution of fluctuations and the total average energy. In another hand, in the poly-domain around 210 K it can be detected the emergence of a low dimensional dynamics.

5.5 Summing up

Using echo-pulse measurement techniques it was possible to detect an anomaly in the elastic constants of $CaTiO_3$ around 200 K. Molecular dynamics simulations showed that no phase transition occurred in the low temperature range, as confirmed by the pair correlation function and the angle distribution function. The bulk modulus is lower in the poly-domain configuration than in the mono-domain configuration. An anomalous increase in the bulk modulus around 210 K is observed in the poly-domain system, in good agreement with experiments. The structural and dynamical analysis point out to dynamical phenomena rather than a structural change as the cause of the anomaly. The power spectrum of the energy temporal series shows a change of pattern that indicated an increase in the complexity of the dynamics around 210 K. Fluctuations are stronger in the poly-domain configuration and they follow a power law in both configurations. The reconstruction of the dynamics of these systems by a time delay method shows marked differences in mutual information, embedding dimension and correlation dimension around this temperature.

Chapter 6. Extrinsic dielectric contribution: collective model

Molecular dynamics simulation of dielectric response is a promising powerful tool and still evolving field. However, electric interactions are long range interaction and current samples ranges from few nanometers to micrometers. Thus, realistic simulation must include large systems and computational expensive algorithms to appropriately handle long range interactions. Considering the domain structure of ferroelectrics is possible to develop simple collective models. These models can be treated analytically, and they result very convenient to simulate nonlinear dielectric response. Of course, with this approach we loss the wonderful detailed information supply by molecular dynamics, but in compensation we get simple analytical expressions that can be fitted to experimental data to obtain information of the microscopic structure. In this final chapter are discussed two models of collective motion for domain walls motion.

6.1 Domain wall as stretched membrane

Dielectric properties of ferroelectrics are strongly dependent of the domain structure and domain walls mobility. Dielectric permittivity as a function of frequency and temperature are probably the most extensively investigated properties in ferroelectrics, both theoretically and experimentally. In contrast, the dielectric response as function of a dc electric field (bias) has been less studied due to, for one side to sometimes technical difficulties to apply high electric fields in the samples, and on the other side, to the lack of a model to describe the dielectric response for a wide range of electric fields strength [50-54]. The study of the nonlinear dielectric characteristics of ferroelectrics under electric field can provide useful information on the basic physics of ferroelectric domain reorientation and tunability. In this section, a membrane model is proposed in order to describe the domain wall dynamics supposing a general nonlinear dependence of the membrane tension with respect to the stretching generated by an applied external dc electric field.

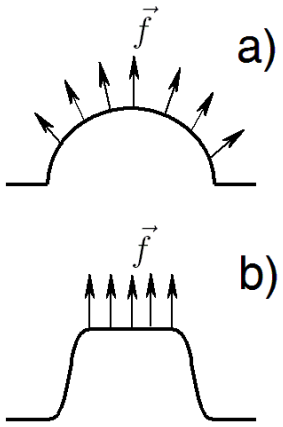

Figure 6.1 a) Membrane under hydrostatic pressure and b) under uniaxial force.

6.1.1 The model

In ferroelectrics the domain wall width is in the order of a few unit cell sizes. As an interface, with thickness and volume much smaller than that of the domains, domain wall can be imagined as a membrane that can be displaced by the action of an external field, as a consequence of domain reorientation. Such reorientation creates tension in the membrane that modifies its mechanical properties. Membranes oscillations are commonly described by nonlinear partial differential equation which, in general, could be very complicate to solve [55-57].

When a hydrostatic pressure is applied in one side of a plane membrane with fixed edges it deforms as a shell due to the force acts normal to the surface (Figure 6.1a). In contrast, when the force in the membrane is uniaxial it remains almost flat, i.e., it suffers a piston like displacement. This is the case of an external electric field E_0 applied to a ferroelectric, in which the electrode areas are much larger than those of the domain walls, so that the exerted force can be considered uniaxial (Figure 6.1b). Based on this assumption it will be assumed that a domain wall behaves as a square membrane under a uniaxial force, generated by an electric field E_0. To determine the domain wall dynamic response a probing field $E_1 \sin\omega t$, with E_1 sufficient weak, superimposed to the dc bias field will be also taken into account.

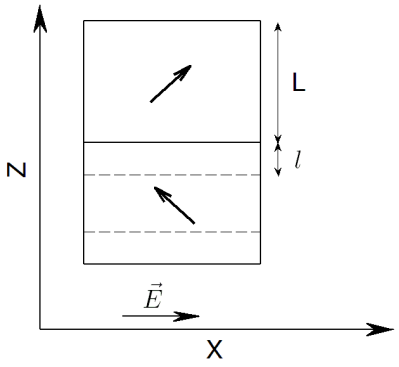

Figure 6.2 Domain wall displacement at a distance l from equilibrium position by the action of external electric field E.

For sake of simplicity, it will be considered a grain formed by an even number of 90º domains under an uniform electric field $E = E_0 + E_1 \sin\omega t$. Taking a rectangular system of coordinate with XY plane parallel to the membrane plane, the transverse deformation l of the membrane (Figure 6. 2) can be decomposed in two components

$$l(t) = l_0 + l_1(t) \tag{6.1}$$

where l_0 is the deformation caused by E_0 and $l_1(t)$ is due to the alternating component $E_1 \sin\omega t$. As E_1 is assumed weak then $l_1(t)$ can be considered small. The small transverse oscillations are described by the boundary value problem [58]:

$$\frac{\partial^2 l_1}{\partial t^2} = a^2\left(\frac{\partial^2 l_1}{\partial x^2} + \frac{\partial^2 l_1}{\partial y^2}\right) - \lambda\frac{\partial l_1}{\partial t} + \frac{2P_{\|}E_1}{\rho}\sin\omega t \tag{6.2}$$

$$l_1(0,y,t) = 0, l_1(b,y,t) = 0, l_1(x,0,t) = 0, l_1(x,b,t) = 0 \tag{6.3}$$

where b is the length of the non-deformed membrane, λ a damping coefficient, ρ the effective mass per unit of area of the wall, $a^2 = T(E_0)/\rho$ with $T(E_0)$ the membrane tension which is a positive monotonically increasing function of E_0, and $P_{\|}$ is the polarization component of P_0 along the Z axis. It is assume that the applied field E is in the X −direction.

The inclusion of the last term in equation (6.2) can be explained as follows. Consider a cylinder with height 2L (L is the thickness of the domains when no external field is acting), and top and bottom surfaces δA parallel to the domain walls (Figure 6.2). The dipole moment enclosed by the cylinder is $\Delta d = 2l\delta A P_0$. The electrostatic energy due to the interaction with the electric field $E_1 \sin\omega t$ is $\Delta U = -2l\delta A P_{\|} E_1 \sin\omega t$. Hence, the force per unit area that acts in the membrane is $\frac{-1}{\delta A}\frac{\partial \Delta U}{\partial l} = 2P_{\|} E_1 \sin\omega t$.

The steady-state solution of this linear boundary problem can be found by the method of separation of variables and it is given by [58, 59]:

$$l_1(x,y,t) = \frac{-32P_0E_1}{\rho\pi^2}\sum_{i,j=0}^{+\infty}\frac{\left(\omega^2-\omega_{ij}^2\right)\sin\omega t+\lambda\omega\cos\omega t}{(2i+1)(2j+1)\left[\left(\omega^2-\omega_{ij}^2\right)^2+\lambda^2\omega^2\right]}\sin\left[\frac{(2i+1)\pi x}{b}\right]\sin\left[\frac{(2j+1)\pi y}{b}\right] \quad (6.4)$$

$$\omega_{ij}^2 = \left(\frac{\pi a}{b}\right)^2[(2i+1)^2+(2j+1)^2] = \frac{\omega_{00}^2}{2}[(2i+1)^2+(2j+1)^2] \quad (6.5)$$

As the parameter $a = \sqrt{T(E_0)/\rho}$ is a function of the bias field E_0 then $\omega_{ij} = \omega_{ij}(E_0)$. The total polarization is:

$$P(t) = \frac{2P_0l_0}{L} + \frac{2P_0\int_0^b\int_0^b l_1(x,y,t)dxdy}{b^2L} \quad (6.6)$$

From equation (6.6) we can find the real and imaginary permittivity as:

$$\varepsilon' = \varepsilon'_{00} + \delta\varepsilon'(E_0,\omega), \qquad \delta\varepsilon'(E_0,\omega) = \frac{P'(E_0,\omega)}{\varepsilon_0E_1(\omega)} \quad (6.7)$$

$$\varepsilon'' = \varepsilon''_{00} + \delta\varepsilon''(E_0,\omega), \qquad \delta\varepsilon''(E_0,\omega) = \frac{P''(E_0,\omega)}{\varepsilon_0E_1(\omega)} \quad (6.8)$$

where ε_0 is the vacuum dielectric permittivity, $P'(E_0,\omega)$ and $P''(E_0,\omega)$ are given by

$$P'(E_0,\omega) = \frac{\omega}{\pi}\int_0^{2\pi/\omega}P(t)\sin\omega t dt, \quad P''(E_0,\omega) = \frac{\omega}{\pi}\int_0^{2\pi/\omega}P(t)\cos\omega t dt \quad (6.9)$$

The terms ε'_{00} and ε''_{00} are the contribution of other polarization mechanism to the real and imaginary permittivity, respectively. We will consider ε'_{00} approximately constant for not so high electric fields (experimentally attainable). From the solution given by equation (6.4) and the expressions (6.6)- (6.9) we have:

$$\varepsilon'(E_0,\omega) = \varepsilon'_{00} + \frac{256P_\parallel^2}{\varepsilon_0\rho L\pi^4}\sum_{i,j=0}^{+\infty}\frac{\omega_{ij}^2-\omega^2}{(2i+1)^2(2j+1)^2\left[\left(\omega_{ij}^2-\omega^2\right)^2+\lambda^2\omega^2\right]} \quad (6.10)$$

$$\varepsilon''(E_0,\omega) = \varepsilon''_{00} + \frac{256P_\parallel^2}{\varepsilon_0\rho L\pi^4}\sum_{i,j=0}^{+\infty}\frac{\lambda\omega}{(2i+1)^2(2j+1)^2\left[\left(\omega_{ij}^2-\omega^2\right)^2+\lambda^2\omega^2\right]} \quad (6.11)$$

According to this result there is an infinite set of resonance frequencies. However, experimentally most of the time only one over damped (relaxation like) characteristic frequency is observed, it depends on the damping coefficient. For small values of the damping coefficient ($\lambda < \omega_{00}$) secondary resonances weakly appear, as is shown in Figure 6.3a; while for $\lambda > \omega_{00}$ they can be neglected, and a

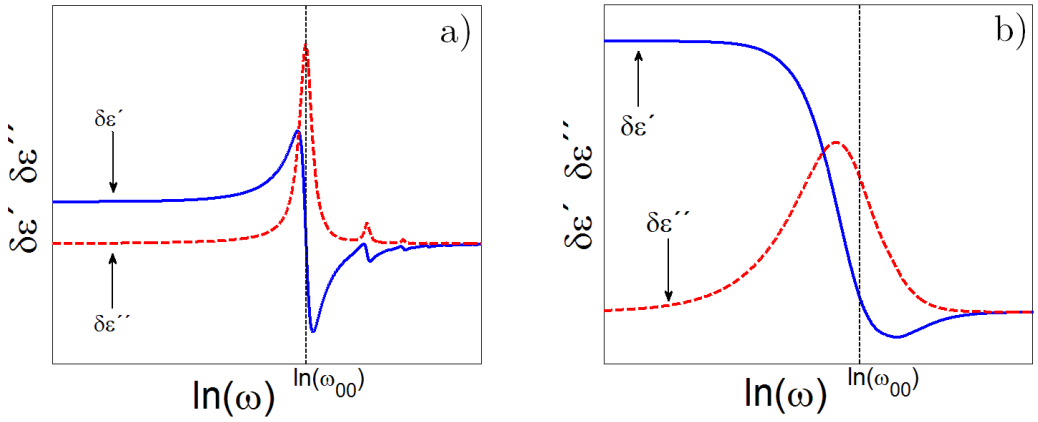

Figure 6.3 Frequency dependence of real (solid line) and imaginary (dash line) dielectric permittivity for different damping coefficient λ: a) $\lambda < \omega_{00}$ and b) $\lambda > \omega_{00}$.

relaxation like response is obtained (Figure 6.3b). Typical experimental value for the damping coefficient, determined for several materials, is $\lambda \approx 2\omega_{00}(0)$ [60].

For low frequencies regime ($\omega \ll \omega_{00}$) equations (6.10) and (6.11) can be approximated by

$$\varepsilon'(E_0,\omega) \approx \varepsilon'_{00} + \frac{GS_1}{\omega_{00}^2(E_0)} \tag{6.12}$$

$$\varepsilon''(E_0,\omega) \approx \varepsilon''_{00} + \frac{2G\omega\lambda S_2}{\omega_{00}^4(E_0)} \tag{6.13}$$

with

$$G = \frac{512P_{\parallel}^2}{\rho L\pi^4} \tag{6.14}$$

$$S_1 = \sum_{i,j=0}^{+\infty} \frac{1}{(2i+1)^2(2j+1)^2[(2i+1)^2+(2j+1)^2]} \tag{6.15}$$

and

$$S_2 = \sum_{i,j=0}^{+\infty} \frac{1}{(2i+1)^2(2j+1)^2[(2i+1)^2+(2j+1)^2]^2} \tag{6.16}$$

Normalizing equation (6.12) it stands as:

$$\frac{(\varepsilon'-\varepsilon'_{00})}{\varepsilon_{Max}} = \frac{GS_1}{\omega_{00}^2(E_0)\varepsilon_{Max}} \tag{6.17}$$

where

$$\varepsilon_{Max} \equiv Max(\varepsilon'(E_0,0)\,) \tag{6.18}$$

The numerical series S_1 and S_2 converge very fast and their approximate values are $S_1 \cong 0.528$ and $S_2 \cong 0.252$.

The experimental curve $\varepsilon'(E_0)$ can be fitted by an appropriate empirical relationship. The most important phenomenological approach to this problem is the Landau-Ginzburg-Devonshire (LGD) theory [53, 61, 62]. The main difficulty of this formulation is that it does not provide an explicit expression for $\varepsilon'(E_0)$. Based in the LGD theory, Johnson [61] obtained an approximated relation that fits the dependence of permittivity with electric field on the paraelectric phase [53, 61]. The Johnson approximation works well for moderate electric fields and it does not reproduce hysteretic behavior of ferroelectrics.

For ferroelectrics in paraelectric phase, using the LGD theory, it is possible to demonstrate the dependence $\varepsilon' \sim 1/(\alpha + \beta E^2)$ where α and β are functions of temperature. A similar empirical law was introduced by Rupprecht *et al.* [63] to describe the nonlinear dielectric behavior of $SrTiO_3$. This expression can be generalized to describe the nonlinear behavior of ferroelectrics and hysteretic effect [64] through the effective field E_{eff} :

$$\frac{(\varepsilon' - \varepsilon'_{00})}{\varepsilon_{Max}} \approx \frac{1}{\alpha + \beta E_{eff}^2} \tag{6.19}$$

$$E_{eff} \equiv E_0 + \kappa P(E_0) \tag{6.20}$$

where α and β that depend on the structure and are also function of temperature, parameter κ is a generalization of Lorentz factor [53] depending on the geometry of the domains and characteristic length scales (texture, shape and grain size, among others).

Comparing equation (6.17) and (6.19)-(6.20) results:

$$\omega_{00}^2(E_0) = \frac{GS_1}{\varepsilon_{Max}}[\alpha + \beta(E_0 + \kappa P(E_0))^2] \tag{6.21}$$

Inserting equation (6.21) in (6.5) we have

$$\omega_{ij}^2(E_0) = \frac{GS}{2\varepsilon_{Max}}[(2i+1)^2 + (2j+1)^2][\alpha + \beta(E_0 + \kappa P(E_0))^2] \tag{6.22}$$

If $P(E_0)$ and the characteristic frequency $\omega_{00}(0)$ are known then the other parameters could be determined from the curve $\varepsilon'(E_0)$ and for low frequencies the dispersion relationships could be evaluated directly from equations (6.12) and (6.13).

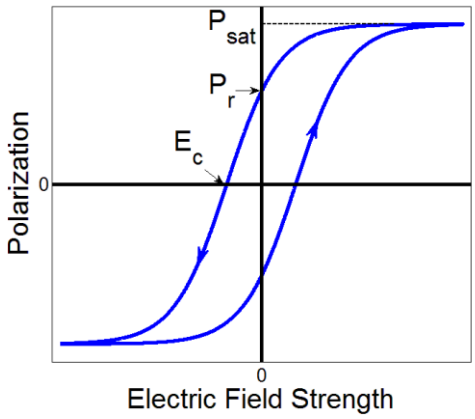

Figure 6.4 Ferroelectric hysteresis loop.

6.1.2 Hysteretic consideration

It is well known that under the action of an electric field, higher than the coercive field E_c, the polarization in normal ferroelectrics can be reoriented. The reorientation of the macroscopic polarization in ferroelectrics is a hysteretic process. In order to generalize our model to correctly describe the $\varepsilon'(E_0)$ response in normal ferroelectrics, the hysteretic electric field dependence of the macroscopic polarization can be included in the model through a contribution to the effective field in the equations (6.19) and (6.20). The hysteretic behavior of the polarization can be modeled by the mathematical relation [50, 51]:

$$P = P_{sat}\tanh[(E_0 \pm E_c)/2\delta] \tag{6.23}$$

$$\delta = E_c\left[\ln\left(\frac{1+P_r/P_{sat}}{1-P_r/P_{sat}}\right)\right]^{-1} \tag{6.24}$$

where E_c is the coercive field, P_{sat} the saturation polarization and P_r remanent polarization (Figure 6.4).

Inserting equation (6.23) in (6.21) we obtain

$$\omega_{00}^2(E_0) = \frac{GS_1}{\varepsilon_{Max}}\{\alpha + \beta[E_0 + \kappa P_{sat}\tanh((E_0 \pm E_c)/2\delta)]^2\} \tag{6.25}$$

inserting equation (6.25) in (6.17) results

$$\frac{(\varepsilon' - \varepsilon'_{00})}{\varepsilon_{Max}} = \frac{1}{\alpha+\beta\{E_0+\kappa P_{sat}\tanh[(E_0\pm E_c)/2\delta]\}^2} \tag{6.26}$$

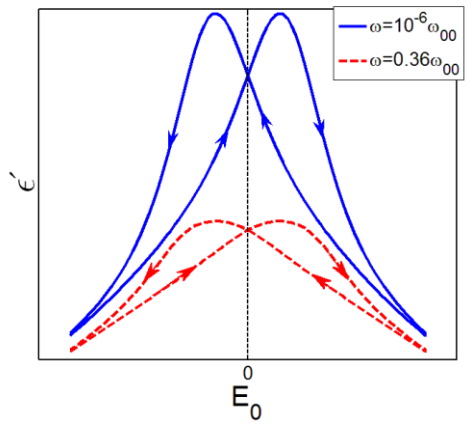

Figure 6.5 Dielectric permittivity versus electric field strength due to hysteretic effect. Dispersion is notable for high frequencies($\omega \sim \omega_{00}$).

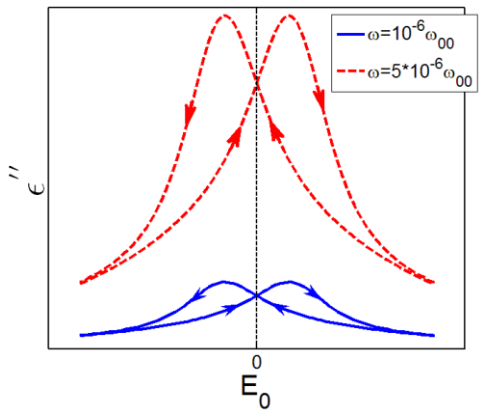

Figure 6.6 Imaginary part of dielectric permittivity versus bias electric field involving polarization switching.

The inclusion of the ferroelectric hysteresis in the model allows reproducing the hysteretic response of $\varepsilon'(E_0)$ and $\varepsilon''(E_0)$ curves as they are typically observed in experimental data, Figures 6.5 and 6.6. For frequencies around $\omega \sim \omega_{00}$ dispersion can be observed in the curves $\varepsilon'(E_0)$, similar as it is observed experimentally [65]. Conversely, imaginary part of permittivity grows with the increment of the frequency as it is shown in Figure 6.6.

As the coercive field becomes smaller the peaks in the $\varepsilon'(E_0)$ curve become closer together, overlapping as E_c is negligible (Figure 6.7). Using the condition of extreme and supposing that $\kappa > 0$ in the equation (6.26) the κ parameter can be determined. For the right hand branch of a curve $\varepsilon'(E_0)$ we find that

$$\kappa = \frac{-\tilde{E}}{P_s \tanh[(\tilde{E}-E_c)/2\delta]} \tag{6.27}$$

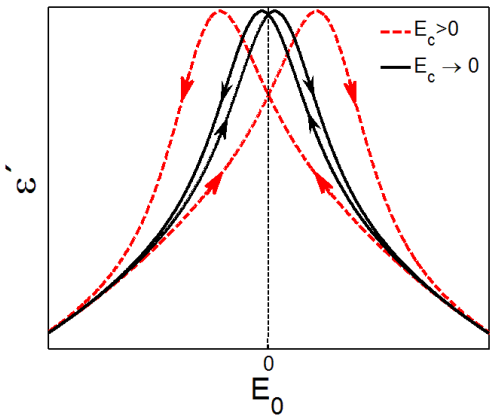

Figure 6.7 As E_c diminishes both curves tend to overlap.

where $\widetilde{E}$ is the value of E_0 for which $\varepsilon'(E_0)$ reach its maximum value (the peak in the $\varepsilon'(E_0)$ curve). Notice from equation (6.26) that the maximum of $\varepsilon'(E_0)$ occurs for $\widetilde{E} < E_c$.

6.1.3 Reconstruction of hysteresis loop from the CV curve

Common bulk ferroelectrics behave as insulators. In thin film several conduction mechanisms appear and they smear the polarization loop. In conductive sample the hysteresis loop shows a typical banana shape, this is due that depolarization current is accompany by the conductive currents. Integrating the relation $\varepsilon' = 1 + \frac{1}{\epsilon_0}\frac{dP}{dE}$ with respect to the field, we can find P(E). But the curve obtained by the integration of the experimental curve $\varepsilon'(E)$ is different from the experimental curve obtained by direct measurement [2]. This occurs because both curves are obtained for different experimental conditions. The curve $\varepsilon'(E)$ is measured using a constant field E_0 and a weak alternating field E_1, while the hysteresis loop P(E) is measured using a strong alternating electric field.

According to our model the curve $\varepsilon'(E)$ contains the information of the hysteresis loop. From the fitting of $\varepsilon'(E)$ using equation (6.26) we can extract the parameters E_c and δ. Now we will deduce an expression to calculate the saturation polarization. The hysteresis model given by equation (6.23) can be generalized including a linear term, i.e.:

$$P(E) = \varepsilon_0\chi_{00}E_0 + P_{sat}\tanh[(E_0 \pm E_c)/2\delta] = \varepsilon_0\chi_{00}E_0 + P_{hyst}(E) \qquad (6.28)$$

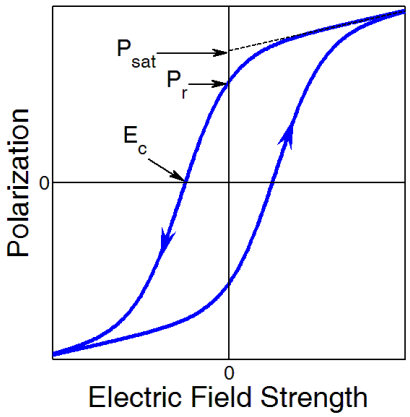

Figure 6.8 Hysteresis loop with a linear contribution.

The term $\varepsilon_0\chi_{00}E_0$ can be interpreted as an approximation to the contribution of intrinsic polarization mechanism (ionic, electronic, etc). This hysteresis loop model (Figure 6.8) is a generalization of the previous given by equation (6.23). In the cases that $\varepsilon_0\chi_{00}E_{max} \ll P_{sat}$, where E_{max} is the maximum attainable electric field, equation (6.28) reduces to (6.23).

Now we will consider an electric field $E(t) = E_0 + E_1 \sin\omega t$, where E_0 is constant or vary very slowly and E_1 is weak. Then expanding around E_0 in power series

$$P(E_0 + E_1\sin\omega t) = \varepsilon_0\chi_{00}(E_0 + E_1\sin\omega t) + P_{hyst}(E_0) + \frac{dP_{hyst}(E_0)}{dE}E_1\sin\omega t + \cdots$$

Dropping power of $E_1\sin\omega t$ higher than 1 and expanding in Fourier series

$$P(\omega) \approx \varepsilon_0\chi_{00}E_1 + \frac{dP_{hyst}(E_0)}{dE}E_1$$

Thus, the electric displacement in frequency domain can be written as

$$D(\omega) = \varepsilon_0 E(\omega) + P(\omega) \cong \varepsilon_0 E(\omega) + \varepsilon_0\chi_{00}E(\omega) + \frac{dP_{hyst}(E_0)}{dE}E(\omega) \qquad (6.29)$$

Notice that $E(\omega) = E_1$. Comparing (6.29) with the state equation

$$D(\omega) = \varepsilon_0\varepsilon(\omega, E_0)E(\omega) = \varepsilon_0[\varepsilon_{00} + \delta\varepsilon(E_0)]E(\omega) \qquad (6.30)$$

We obtain

$$\frac{dP_{hyst}(E_0)}{dE} = \varepsilon_0[\varepsilon(\omega, E_0) - \varepsilon_{00}]$$

From which, integrating, we get that

$$2P_{sat} = \int_{-\infty}^{+\infty} \varepsilon_0[\varepsilon(\omega, E) - \varepsilon_{00}]dE \qquad (6.31)$$

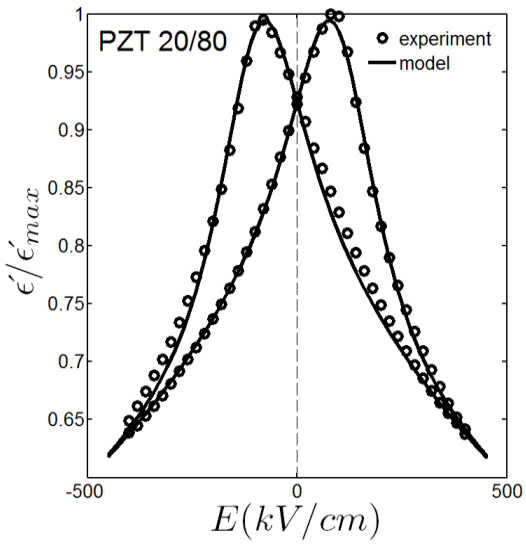

Figure 6.9 Real dielectric permittivity vs. bias electric field strength for $PZr_{0.8}Ti_{0.2}O_3$ (circles) and inverse quadratic model (solid line). Fitting was performed for the right hand-side branch of the curve. All the measurements were performed at a frequency of 100 kHz (probing field).

The model was tested using experimental data obtained from the $PZr_{0.8}Ti_{0.2}O_3$ (PZT 20/80) and $PZr_{0.53}Ti_{0.43}O_3$ (PZT 53/47) thin films prepared by a chemical procedure and deposited on $Pt/Ti/SiO_2/Si$ substrates. Measurements were performed at room temperature and probing field with a frequency of 100 kHz (which is far below the characteristic frequency $\omega_{00}(0)$ for these films).

Figure 6.9 shows the curve $\varepsilon'(E_0)$ obtained for PZT 20/80 thin film. The experimental data (represented by circles) was fitted by the equation (6.26) using the Levenberg-Marquardt algorithm. All the parameters where taken as unknown. The fitting was made using the curve branch corresponding to the right hand-side peak. As it can be seen in Figure (6.9) an excellent concordance is achieved between experimental data and model. From the numerical fitting it was obtained: $\varepsilon'_\infty/\varepsilon_{Max} = 0.33728$, $\alpha = 1.52045$, $\beta = 2.91108 * 10^{-6}$cm/kV, $\kappa P_{sat} = 387.7$ kV/cm, $E_c = 104.27$ kV/cm and $2\delta = 135.84$ kV/cm.

From equations (6.26) and (6.31) is obtained for the PZT20/80 thin film $P_{sat} = 11.74\ \mu C/cm^2$. Figure 6.10 shows (solid line) the experimental hysteresis loop and the reconstructed hysteresis loop (dash line). From experimental curves we got $\widetilde{E} = 80$ kV/cm and $E_c \approx 120$ kV/cm , confirming the fact that $\widetilde{E} < E_c$ as it is predicted by the model.

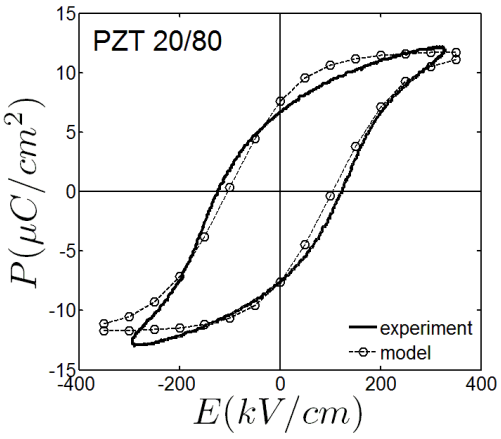

Figure 6.10 $PbZr_{0.8}Ti_{0.2}O_3$ hysteresis loop (solid line) and the reconstructed loop from $\varepsilon'(E_0)$curves (circles).

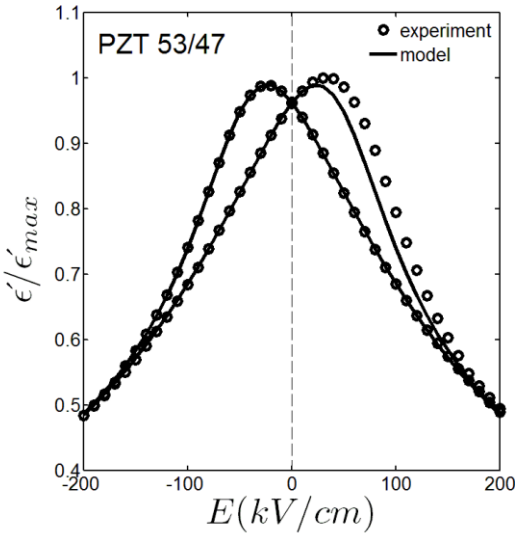

Figure 6.11 Real permittivity versus electric field strength for $PbZr_{0.53}Ti_{0.43}O_3$.

Following the same procedure, the curve obtained for the PZT 53/47 thin film was fitted with the expression (6.26) using the data from the left hand side branch (Figure 6.11). Also in this case, an excellent agreement between experimental data and fitting is observed. From the numerical fitting resulted: $\varepsilon'_\infty/\varepsilon_{\mathrm{Max}} = 0.179$, $\alpha = 1.23$, $\beta = 31.34 * 10^{-6}$cm/kV, $\kappa P_{sat} = 54.8$ kV/cm, $E_c = 54.8$ kV/cm and $2\delta = 66.5$ kV/cm.

In Figure 6.12 are presented the experimental and reconstructed hysteresis loops for the PZT 53/47 thin film. It can be observed that the experimental polarization saturation is much higher than that obtained from the $\varepsilon'(E_0)$ curve. This difference is due to the nonlinear conductive contribution which is present in the experimental loop.

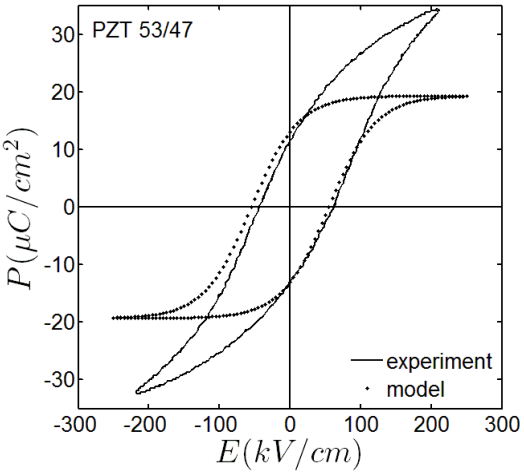

Figure 6.12 $PbZr_{0.53}Ti_{0.43}O_3$ hysteresis loop (solid line) and the reconstructed loop from $\varepsilon'(E_0)$ curves (circles). The divergence is attributed to the conduction current.

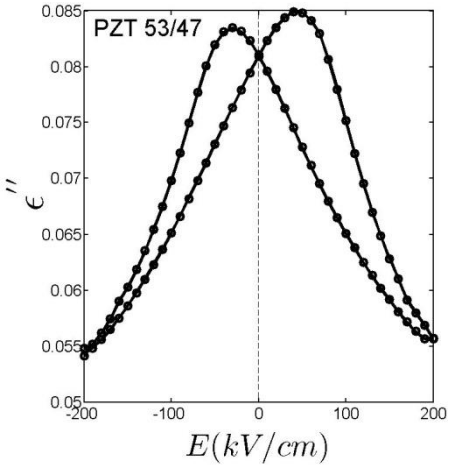

Figure 6.13 Imaginary permittivity versus bias electric field strength for $PbZr_{0.53}Ti_{0.43}O_3$.

The frequency ω_{00} is estimated from the curve $\varepsilon''(E_0)$ (Figure 6.13) using the parameters found by the fitting of ε'vs. E_0 curve. From equation (6.25) and making $E_0 = 0$ we got

$$G = \frac{\omega_{00}^2(0)\varepsilon_{Max}}{S_1\{\alpha+\beta[kP_{Sat}\tanh(E_c/2\delta)]^2\}} \tag{6.32}$$

Substituting equation (6.25) and (6.32) in (6.13) and making $\lambda = 2\omega_{00}$ we have:

$$\varepsilon'' = \varepsilon''_{00} + \frac{g}{\langle\alpha+\beta\{E_0+\kappa P_{sat}\tanh[(E_0\pm E_c)/2\delta]\}^2\rangle^2} \tag{6.33}$$

$$g = (4S_2\omega\varepsilon_{Max}/\omega_{00}S_1)\{\alpha + \beta[kP_{Sat}\tanh(E_c/2\delta)]^2\} \tag{6.34}$$

For the real permittivity we have $\varepsilon_{Max} = 1010.6$ and $\omega = 100$ kHz. Fitting of imaginary permittivity to equations (6.33) and (6.34) we get $\omega_{00} \cong 4.88$ rad/ns (~0.78 GHz), which is in the order of the reported value for this material [60, 65].

In this section, we generalized the hysteresis loop model introduced in the previous section. We will show that this does not affect the result given by equation (6.26). Effectively, inserting equation (6.28) in (6.21) and the result in (6.17) we arise to:

$$\frac{(\varepsilon' - \varepsilon'_{00})}{\varepsilon_{Max}} = \frac{1}{\alpha + \tilde{\beta}\{E_0 + \tilde{\kappa} P_{sat} \tanh[(E_0 \pm E_c)/2\delta]\}^2}$$

where $\tilde{\beta} = \beta(1 + \kappa\varepsilon_0\chi_{00})^2$ and $\tilde{\kappa} = \kappa/(1 + \kappa\varepsilon_0\chi_{00})$. Thus the equation (6.26) retains the same form and the parameters E_c and δ are not affected. Obviously, the saturation polarization calculated from (6.31) is also the same.

6.1.4 Domain size effect

According to equation (6.5) ω_{ij}^2 is inversely proportional to the domain wall size (parameter b). Taking certain value b_0 as a reference we can introduce the dimensionless parameter $\xi \equiv b/b_0$, so that

$$\omega_{00}^2(E_0, \xi) = \omega_{00}^2(E_0)/\xi \qquad (6.35)$$

Considering that domain size is dependent of grain size [8, 66-68] and assuming that there is linear relation between grain and domain wall size, using equations (6.26) and (6.35) it is possible to simulate the effect of domain size on dielectric response. Figure 6.14 shows the dependence of permittivity and its derivative with respect to the electric field for several values of the parameter ξ. The parameters used in the simulation correspond to a PZT 20/80 thin film. The model predicts a diminution of dielectric permittivity and tunability with the decrease of domain size in agreement with experimental observations (see Figure 6.15).

We have limited our discussion to the analysis of grain size effect on the characteristic frequency ω_{00}^2, and dielectric permittivity. In certain materials it is observed that L is proportional to the square root of grain size [8, 66]. In term of the dimensionless parameter ξ the domain width can be expressed as $L \sim \sqrt{\xi}$. As $G \sim 1/L$ and according to the expression (6.17) and (6.35) this implies that $\varepsilon' \sim \sqrt{\xi}$.

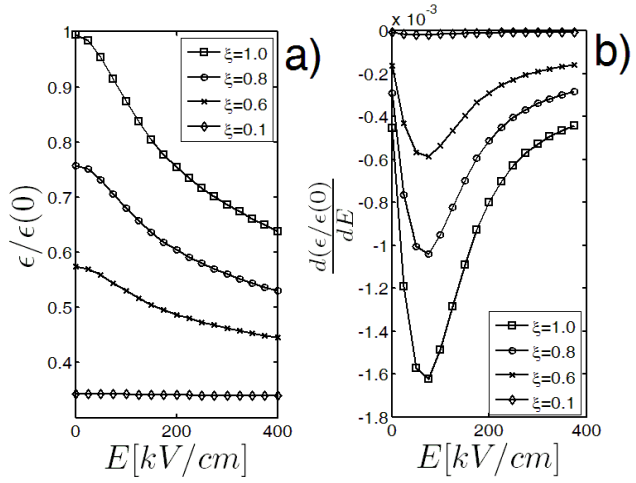

Figure 6.14 a) Simulation of permittivity versus electric field and b) its derivative with respect to the electric field for different membrane size (ξ).

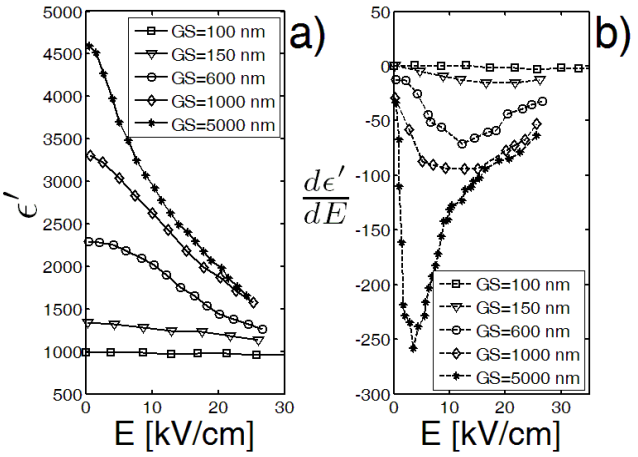

Figure 6.15 a) Permittivity versus electric field and b) its derivative with respect to the electric field of $BaTiO_3$ ceramic with various grain sizes [10].

There are other factors that can affect the dielectric response as the grain size is diminished, such as for example dead layers, which contribution increase as grain size decrease. Padurariu *et al*. [10] explain the same effects considering that both the local electric inhomogeneity and the contribution of low permittivity grain boundaries increase when grain size decreases. It is evident the complexity of this problem due to simultaneous change of several parameters as the grain size is diminished. A way to elucidate the exact role of these mechanisms on the dielectric response and tunability could be achieved by the direct measurement of domains and domain walls sizes, and their dielectric characteristic frequencies.

6.2. Kittel's model

Domain walls motion was modeled by Kittel [69] and other authors [70-73] as a rigid body moving in a dissipative medium in a harmonic potential. Dispersion relationships for real and complex permittivity are obtained from the solution of this equation. Due to the linear nature of this equation, it does not reproduce neither the nonlinear effects of electric field nor transient effects. Here we discussed a model that is a generalization of the original Kittel's equation incorporating a nonlinear potential. Assuming that the permittivity follows the dependence $\varepsilon' \propto 1/(\alpha + \beta E^2)$ it is obtained the exact expression for effective potential. Numerical simulation of polarization current shows that it follows a power law. Such results could be very valuable in the study of domain wall kinetic and ultrafast polarization processes. The model is extended to the case of pole sample allowing the study of nonlinear permittivity behavior for alternating electric field lower than the coercive field.

6.2.1 The model

We will start by considering a ferroelectric grain formed by a periodic array of domains polarized 90° each respect the others (Figure 6.2). Under the action of the electric field $E(t) = E_0 + E_1 \cos(\omega t)$ the domain walls motion equation may be written as:

$$gA\frac{d^2l}{dt^2} = -\frac{dW}{dl} + 2AP_{\parallel}E(t) - gA\lambda\frac{dl}{dt} \tag{6.36}$$

where l is the wall displacement from the equilibrium position, A is the area of the wall, g the effective wall mass per unit of area, λ a damping coefficient, W(l) represent the effective potential, and $P_{\parallel}$ is the component of the polarization in the direction of E(t). The damping is occasioned by the coupling with lattice vibration, local imperfections, acoustic radiation and other causes. The polarization component in the field direction is given by

$$P(t) = \frac{2l}{L}P_{\parallel} \tag{6.37}$$

For an amplitude of alternating field E_1 sufficient small the system perform harmonic oscillation around the equilibrium position l_0:

$$l(t) \cong l_0 + l_{11}\cos\omega t + l_{12}\sin\omega t \tag{6.38}$$

Accordingly to (6.38) the permittivity can be written as

$$\varepsilon' = \varepsilon'_{00} + \delta\varepsilon'(E_0,\omega)\,, \qquad \delta\varepsilon'(E_0,\omega) = \frac{1}{\varepsilon_0 E_1}\frac{\omega}{\pi}\int_0^{2\pi/\omega} P(t)\cos(\omega t)dt \tag{6.39}$$

where ε'_{00} can be taken as a constant, it represents the lattice contribution to dielectric response. The equilibrium position is determined by the equation

$$0 = -\frac{dW}{dl}(l_0) + 2AP_{\|}E_0 \tag{6.40}$$

Certain properties of the function W(l) can be inferred from the response of the system: it must be symmetric function so that the response is the same when the electric field is inverted, the motion must be reversible in the absent of defects (pinning) then W(l) has a unique equilibrium point in the origin, and finally the motion is limited to $\pm L/2$. From these properties we arrive to the conclusion that W(l) is a symmetric infinity potential well with an absolute minimum at the origin.

Expanding equation (6.36) in powers of $y = l - l_0$ up to third degree, and dropping high order terms it becomes in

$$\frac{d^2y}{dt^2} + \lambda\,\frac{dy}{dt} + \Omega^2(l_0)y = e_1\cos\omega t + \mu f(l_0)y^2 + \mu^2 h(l_0)y^3 \tag{6.41}$$

where $\Omega^2(l_0) = \frac{1}{gA}\frac{d^2W(l_0)}{dl^2}$, $f(l_0) = \frac{-1}{2gA}\frac{d^3W(l_0)}{dl^3}$, $h(l_0) = \frac{-1}{6gA}\frac{d^4W(l_0)}{dl^4}$ and $e_1 = \frac{2P_0E_1}{g}$, μ is a formal parameter that indicate the nonlinear term of small absolute value. We will use the small parameter method [74, 75] to obtain the approximate solution of (6.41). The proposed solution has the form

$$y(t) = y_0(t) + \mu y_1(t) + \mu^2 y_2(t) + \cdots \tag{6.42}$$

Inserting (6.42) in (6.41) and equating coefficients of same powers of μ we get

$$y_0'' + \lambda y_0' + \Omega^2 y_0 = e_1\cos\omega t \tag{6.43}$$

$$y_1'' + \lambda y_1' + \Omega^2 y_1 = f y_0^2 \tag{6.44}$$

$$y_2'' + \lambda y_2' + \Omega^2 y_2 = 2f y_0 y_1 + h y_0^3 \tag{6.45}$$

Solving (6.43) we find

$$y_0(t) = \frac{(\Omega^2-\omega^2)e_1}{(\Omega^2-\omega^2)^2+\lambda^2\omega^2}\cos\omega t + \frac{\lambda\omega e_1}{(\Omega^2-\omega^2)^2+\lambda^2\omega^2}\sin\omega t \qquad (6.46)$$

Substituting (6.46) in (6.44) and solving it we get a solution of the kind $y_1(t) = C_{11}\cos\omega t + C_{12}\sin\omega t + C_{10}$, which do not contain the principal frequency. Only in second order approximation reappears the terms containing principal frequency, then we will take (6.46) as the approximate solution. Making $l \cong l_0 + y_0(t)$, inserting in (6.37) and using (6.39) we obtain

$$\varepsilon'(E_0,\omega) = \varepsilon'_{00} + \frac{4P_{\|}^2}{\varepsilon_0 gL}\frac{\Omega^2-\omega^2}{(\Omega^2-\omega^2)^2+\lambda^2\omega^2} \qquad (6.47)$$

This result coincided with that derived from the Kittel's linear model [69] except that $\Omega = \Omega(E_0)$. For low frequencies ($\omega \ll \Omega(0)$) the dispersion relationship (6.47) can be written as

$$\varepsilon'(E_0,\omega) \cong \varepsilon'_{00} + \frac{4P_{\|}^2}{\varepsilon_0 gL\Omega^2} \qquad (6.48)$$

6.2.2 Effective potential

We will assume that the dependence $\varepsilon'(E_0)$ is giving by the relation [63, 64]:

$$\frac{(\varepsilon'-\varepsilon'_{00})}{\varepsilon_{Max}} \approx \frac{1}{\alpha+\beta E_0^2} \qquad (6.49)$$

where ε_{Max} is the maximum value of $\varepsilon'(E_0,0)$. Comparing (6.48) and (6.49) we have

$$\Omega^2(E_0) = \frac{4P_{\|}^2}{\varepsilon_0\varepsilon_{Max}gL}\left[\alpha + \beta {E_0}^2\right] \qquad (6.50)$$

As $\Omega^2 = (1/gA)\, d^2W/dl^2$ and using (6.40) it gives

$$\frac{d^2W}{dl^2} = \frac{4P_{\|}^2 A}{\varepsilon_0\varepsilon_{Max}L}\left[\alpha + \beta\left(\frac{dW}{dl}\right)^2\right] \qquad (6.51)$$

This equation is completed using the fact that W(l) has a minimum at the origin, i.e., $\frac{dw}{dl}(0) = 0$. Solving (6.51) by standard methods we find

$$W(l) = \frac{-\varepsilon_0 \varepsilon_{Max} LA}{\beta} \ln\left|\cos\left(\frac{2P_{\|}\sqrt{\alpha\beta}}{\varepsilon_0 \varepsilon_{Max} L} l\right)\right| \tag{6.52}$$

Imposing the condition $W(\pm L/2) = \infty$ it follows that

$$\frac{2P_{\|}\sqrt{\alpha\beta}}{\varepsilon_0 \varepsilon_{Max} L} \cdot \frac{\pm L}{2} = \frac{\pi}{2} \;\rightarrow\; P_{\|} = \frac{\pi \varepsilon_0 \varepsilon_{Max}}{2\sqrt{\alpha\beta}} \tag{6.53}$$

Making $E_0 = 0$ in (6.50) and using (6.53) we get that

$$g = \frac{\pi^2 \varepsilon_0 \varepsilon_{Max}}{L\beta\Omega^2(0)} \tag{6.54}$$

Inserting (6.52) into (6.36) and using (6.53) and (6.54) it is obtained

$$\frac{d^2 l}{dt^2} + \lambda \frac{dl}{dt} + \frac{L\Omega^2(0)}{\pi} \tan\left(\frac{\pi l}{L}\right) = \frac{L\Omega^2(0)}{\pi} \sqrt{\frac{\beta}{\alpha}} E(t) \tag{6.55}$$

Making $z = 2l(t)/L$ in (6.55) and (6.37) they can be written as:

$$\frac{d^2 z}{dt^2} + \lambda \frac{dz}{dt} + \frac{2\Omega^2(0)}{\pi} \tan\left(\frac{\pi}{2} z\right) = \frac{2\Omega^2(0)}{\pi} \sqrt{\frac{\beta}{\alpha}} E(t) \tag{6.56}$$

$$P(t) = z(t) P_{\|} \tag{6.57}$$

The parameters α and β can be found from the curve $\varepsilon'(E)$ [30], while $\Omega(0)$ is determine from the curve $\varepsilon'(\omega)$. The damping coefficient also can be found experimentally from the curves $\varepsilon'(\omega)$ and $\varepsilon''(\omega)$.

6.2.3 Time–domain relaxation

By means of equations (6.56) and (6.57) it is possible to simulate the transient currents for arbitrary input signal lower than coercive field. The Figure 6.16 shows simulations of polarization for different external fields, the parameters used in the simulation where obtained from PZT 20/80 [64]. Such simulations agree with the observed behavior in ultrafast polarization process for low input signal in thin films. As it is shown in Figure 6.17, the numerical simulations correctly predict a power law for

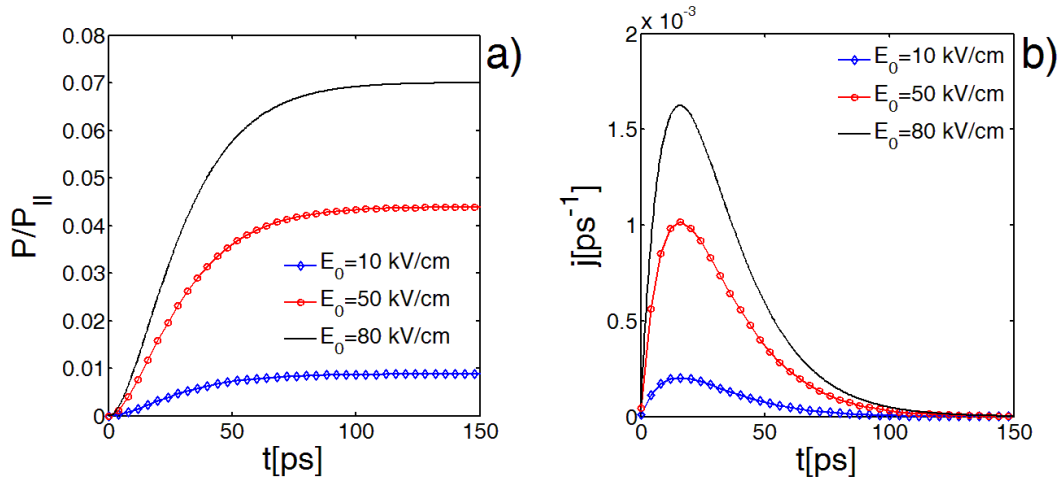

Figure 6.16 Polarization transient at different external fields: $\alpha = 1.5, \beta = 3 \cdot 10^{-6}\ \mathrm{cm^2/kV^2}$, $\lambda = 2\Omega(0)$ and $\Omega(0) = 4.39\ \mathrm{rad/ns}(\sim 0.7\ \mathrm{GHz})$.

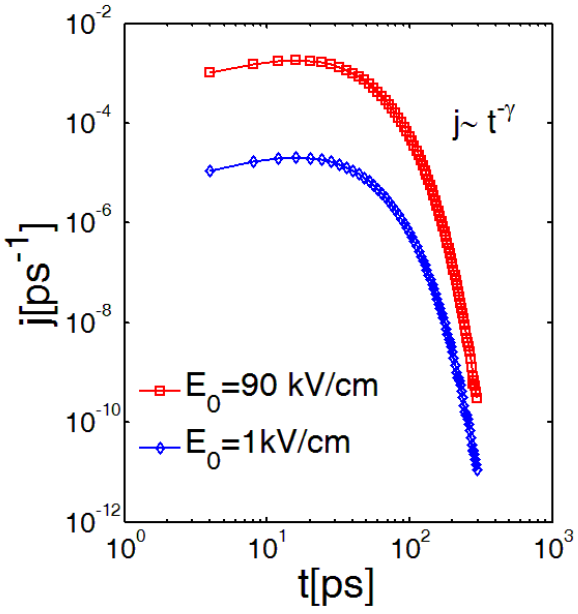

Figure 6.17 Polarization current in double logarithm scale: $E_0 = 100$ kV/cm, the other parameters are the same as in Figure 6.16.

the polarization current $j = -dz/dt \sim t^{-\gamma}$ (polarization current is defined as $J = -dP/dt$ then $J = j * P_{||}$). Power law in dielectric relaxation is a well establish experimental fact [76, 77]. It is a universal phenomenon that appears for different polarization mechanism [76-81] with the only common feature that it occurs on many body interacting systems.

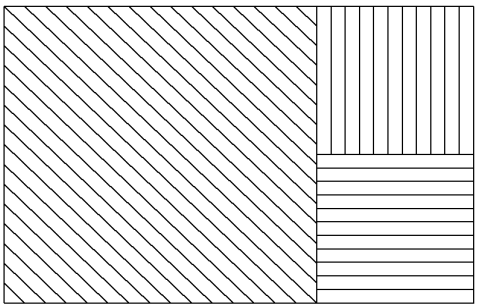

Figure 6.18 Schematic representation of domain structure in a ferroelectric.

6.2.4 Nonlinear dielectric response

Equation (6.55) describes the dynamic of domain wall displacement for a single laminated grain and moderate electric field strength so that the system configuration remains unaltered. Then it could be useful for few nanometers devices with a laminar domain structure. A common bulk ferroelectric sample have domain structure similar to a mosaic in which each region is a system of laminate domains with certain orientation, similar as is shown in Figure 6.18. In a non pole sample the domains are oriented at random. For sufficient strong fields the landscape is altered and the orientations of the regions change. The reorientation of domain is an irreversible process and it cannot be treated with the present formulation.

The structural heterogeneity can be introduced on the model by means of the local field

$$E \rightarrow E_{local} = E + \kappa P(E) \tag{6.58}$$

where κ is a geometric factor.

There are certain cases for which the functional dependence $P(E)$ is known. For an alternating field of low frequencies $\omega \ll \Omega(0)$ and amplitude higher that coercive field the polarization describes a hysteresis loop that can be modeled mathematically as:

$$P = P_{sat}\tanh[(E_0 \pm E_c)/2\delta] \tag{6.23}$$

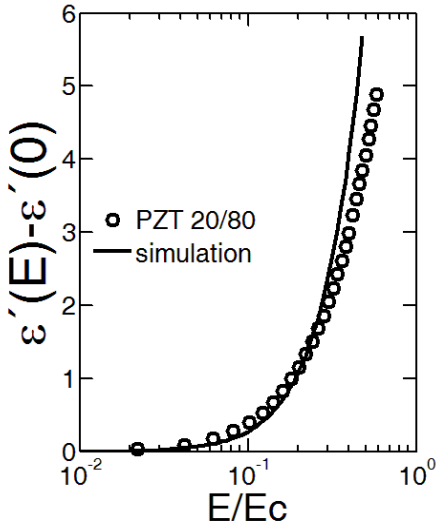

Figure 6.19 Simulated and experimental data of nonlinear response of thin film PZT 20/80 for subswitching fields.

$$\delta = E_c\left[\ln\left(\frac{1+P_r/P_{sat}}{1-P_r/P_{sat}}\right)\right]^{-1} \tag{6.24}$$

where E_c is the coercive field, P_{sat} the saturation polarization and P_r remanent polarization. Using (6.23) and (6.24) in (6.56) we have

$$\frac{d^2z}{dt^2} + \lambda\frac{dz}{dt} + \frac{2\Omega^2(0)}{\pi}\tan\left(\frac{\pi}{2}z\right) = \frac{2\Omega^2(0)}{\pi}\sqrt{\frac{\beta}{\alpha}}\{E(t) + \kappa P_{sat}\tanh[(E(t) \pm E_c)/2\delta]\} \tag{6.59}$$

$$P(t) = z(t)P_{sat} \tag{6.60}$$

Note that we have replaced $P_{\|}$ with P_{sat}. This is due that in the polarized sample still remains certain disorder, then each laminar region has its own polarization component $P_{\|}$. As average we take $P_{sat} \cong \langle P_{\|}\rangle$. Equation (6.59) and (6.60) allow simulating transient effects for electric fields lower than coercive field.

Other important application could be in the simulation of nonlinear behavior of permittivity under alternating electric field also lower than coercive field. This could be very attractive because such response represents domain wall contribution without the effect of defects (pinning). Figure 6.19 shows a simulation of dielectric permittivity for different amplitude of the alternating electric field. The parameters used in the simulation were taken from the fitting of the curve $\varepsilon'(E)$ for PZT 20/80 thin film [64]. It must be emphasized that the parameters have not been adjusted to fit the experimental data.

6.2.5 Derivation of the $\boldsymbol{\varepsilon(E)}$ for low frequencies

For $\omega \ll \Omega(0)$ the derivatives in (6.59) can be neglected and

$$\tan\left(\frac{\pi l}{L}\right) = \sqrt{\frac{\beta}{\alpha}}\{E(t) + \kappa P_{sat}\tanh[(E(t) \pm E_c)/2\delta]\} \tag{6.63}$$

Using (6.63) on $\Omega^2 = (1/gA)\, d^2W/dl^2$ we have that

$$\Omega^2(E) = \Omega^2(0)\,\langle 1 + \frac{\beta}{\alpha}\{E + \kappa P_{sat}\tanh[(E(t) \pm E_c)/2\delta]\}^2\rangle \tag{6.64}$$

Substituting (6.64) in (6.48) and using (6.53) and (6.54) we arrive to

$$\frac{(\varepsilon' - \varepsilon'_{00})}{\varepsilon_{Max}} = \frac{1}{\alpha + \beta\{E + \kappa P_{sat}\tanh[(E \pm E_c)/2\delta]\ \}^2}$$

This result agrees with a previous one obtained from stretched membrane model.

6.3 Summing up and further works

In this last chapter we have discussed two collective model for domain walls motion, from which it is possible to calculate the extrinsic contribution to dielectric response. From the theoretical point of view they constitute an important contribution to the existing theories of nonlinear response which has remained at phenomenological level in the last fifty years. Due to the simplicity of both models it is possible to obtain analytical expression that correctly describe nonlinear response and predict the influence of different factors in the tunability.

The nonlinear Kittel's model has the advantage, with respect to stretched membrane model, that it is possible to study transient current and nonlinear response for alternating subswitching fields. The study of such model still is not complete and the model must be improved. One the remaining open problem is the irreversibility due to the interaction of domain walls with defects. In future works this problem could be treated using two different approaches: one could be to use perturbations δW of the potential to represent point defects or, the second approach, could be to use a generalized dissipative force as a statistical representation of the loss due to the interaction with defects [82].

Conclusions and outlook

In this thesis two problems related to the elastic and dielectric response of materials with perovskite structure were studied. The first problem concerns with the elastic anomalies observed in $CaTiO_3$ around 200 K. This problem was studied using molecular dynamic simulation and nonlinear time series analysis, with which it was possible to reproduce the anomalous elastic behavior and led us to the following conclusions:

i. Although in the simulations were observed changes in the elastic behavior, bulk modulus, no structural change or abrupt change in the energy or volume of the system were detected. Therefore, the observed anomalies are not a structural phase transition.

ii. At 210 K, in both in the mono-domain and poly-domain configurations, a change in the dynamics with an increase of fluctuations is detected, suggesting the occurrence thermal activate process.

iii. Only in the poly-domain configuration there is a considerable change in the elastic behavior and strong fluctuation. These facts point out to domain wall as responsible for the observed phenomenon. Such anomalies can be explained as the occurrence of avalanches or jerk movement in domain wall due to the accumulation of stress.

It is recommendable, in future works, to use the same potential for a massive system (million or more particles) and without periodic boundaries to study in more detail the occurrence avalanches and the microscopic cause that generate the jerk movement of domain walls. Also, we recommend to probe experimentally the occurrence of a thermal activate process at 210 K in $CaTiO_3$, to which we suggest the use of monocrystalline and polycrystalline samples.

The second problem treated concerns with nonlinear hysteretic dielectric response. Two models were proposed to study the contribution of ferroelectric domain wall motion to the dielectric response. From the analytical and numerical study of these models we conclude:

i. The model of the stretched membrane correctly reproduces the real and imaginary dispersion curves. From the model it is possible to derive an analytic expression that correctly fit the $\varepsilon'(E)$ and $\varepsilon''(E)$ curves, reproducing the

hysteretic behavior (or butterfly effect). From the fitting of ε′(E) curve it is possible to reconstruct the hysteresis loop. This model explains qualitatively the effect of domain size in the dielectric response.

ii. The nonlinear Kittel's model allows the simulation of the ultrafast polarization and depolarization processes, predicting a power law dependence with time in agreement with experiments. Using this model it is possible to simulate nonlinear dielectric response on alternating subswitching electric fields. The dispersion relationships can also be derived analytically. The expression obtain for ε′(E) curve coincide exactly with the expression derived from the stretched membrane model.

iii. The result derived from this two different theoretical approach are compatible and can be used to fit experimental data, for example ε′(E) and ε′′(E) curves, to extract information about the microscopic structure.

iv. Both models can be used to reconstruct hysteresis loop from the measurement of ε′(E). This could be very helpful in the study of nonlinear and hysteretic conduction because the method allows the separation of conduction current from polarization and depolarization currents.

It is important to point out that the nonlinear Kittel's model does not reproduce the irreversible behavior at subswitching fields. The next step should be to introduce the action of defects.

References

[1] GEVORGIAN, S. **Ferroelectrics in Microwave devices, circuits and systems**. London: Springer-Verlag, 2009.

[2] DAMJANOVIC, D. Ferroelectric, dielectric and piezoelectric properties of ferroelectric thin films and ceramics. *Rep. Prog. Phys.*, v. 63, p. 1267-1324, 1998.

[3] SCOTT, J. F. Applications of Modern Ferroelectrics. *Science*, v. 315, p. 954-959, 2007.

[4] LINES, M. E.; GLASS A. M. **Principles and applications of ferroelectrics and related materials**. Clarendon: Oxford, 1979.

[5] NYE, J. F. **Physical Properties of crystals**. Oxford: Oxford University Press, 1985.

[6] MITSUI, T.; TATSUZAKI, I.; NAKAMURA E. **An introduction to the physics of ferroelectrics**. London: Gordon and Breach, 1976.

[7] JOAN, F.; SHIRANE, G. **Ferroelectric crystals**. New York: Pergamon, 1962.

[8] ARLT, G.; HENNING, D.; DE WITH, G. Dielectric properties of fine-grained barium titanate ceramics. *J. Appl. Phys.*, v. 58, p. 1619-1625, 1985.

[9] WASER, R. Dielectric analysis of intergrated ceramic thin film capacitors. *Integr. Ferroelectrics.* v. 15, p. 39-51, 1997.

[10] PADURARIU, L.; CURECHERIU, L.; BUSCAGLIA, V.; MITOSERIU, L. Field-dependent permittivity in nanostructured $BaTiO_3$ ceramic: Modeling and experimental verification. *Phys. Rev. B*, v. 85, p. 224111-9, 2012.

[11] SALJE, E. K. H. Ferroelastic materials. *Ann. Rev. Mater. Res.*, v. 42, p. 1-19 (2012).

[12] HARRISON, R. J.; SALJE, E. K. H. The noise of the needle: Avalanches of a single progressing needle domain in $LaAlO_3$. *Appl. Phys. Lett*. v. 97, p. 021907-3, 2010.

[13] NII, Y.; ARIMA, T.; KIM, H. Y.; MIYAZAKI, S. Effect of randomness on ferroelastic transitions: Disorder-induced hysteresis loop rounding in Ti-Nb-O martensitic alloy. *Phys. Rev. B*, v. 82, p. 214104-7, 2010.

[14] GALLARDO, M. C.; MANCHADO, J.; ROMERO, F. J.; CERRO, J.; SAJE, E. K. H.; A.; VIVES, E.; ROMERO, R.; STIPCICH, M. Avalanche criticality in the martensitic transition of $Cu_{67.64}Zn_{16.71}$ $Al_{15.65}$ shape-memory alloy: A calorimetric and acoustic emission study. *Phys. Rev. B*, v. 81, p. 174102-8 (2010).

[15] SALJE, E. K. H.; KOPPENSTEINER, J.; REINECKER, M.; SCHRANZ, W. Jerky elasticity: Avalanches and the martensitic transition in $Cu_{74.08}Al_{23.13}Be_{2.79}$ shape-memory alloy. *Appl. Phys. Lett.*, v. 95, p. 231908-3, 2009.

[16] SALJE, E. K. H.; DING, X.; ZHAO, Z.; LOOKMAN, T.; SAXENA, A. Thermally activated avalanches: Jamming and the progression of needle domains. *Phys. Rev. B*, v. 83, p. 104109-8, 2011.

[17] RAPAPORT, D. C. **The Art of Molecular Dynamics Simulation.** New York: Cambridge University Press, 1997.

[18] VASHISHTA, P.; RAHMAN, A. Ionic motion in α-AgI. *Phys. Rev. Lett*., v. 40, p. 1337-1340, 1978.

[19] SHIMOJO, F.; EBBSJO, I.; KALIA, R. K.; *et al*. Molecular dynamics simulation of structural transformation in silicon carbide under pressure. *Phys. Rev. Lett*., v. 84, p. 3338-3341, 2000.

[20] EBBSJO, I.; KALIA, R. K.; NAKANO, A.; *et al*. Topology of amorphous gallium arsenide on intermédiate length scales: A molecular dynamics study. *J. Appl. Phys*., v. 87, p. 7708-7711, 2000.

[21] LI, W.; KALIA, R. K.; VASHISHTA, P. Amorphization and fracture in silicon diselenide nanowires: A molecular dynamics study. *Phys. Rev. Lett*., v. 77, p. 2241-2244, 1996.

[22] KALIA, R. K.; NAKANO, A.; OMELTCHENKO A.; VASHISHTA, P.. Role of ultrafine microstructures in dynamic fracture in nanophase silicon nitide. *Phys. Rev. Lett*., v. 78, p. 2144-2147, 1997.

[23] RINO, J. P.; CHATTERJEE A., EBBSJO, I.; KALIA, R., *et al*. Pressure-induced structural transformation in GaAs: A molecular dynamics study. *Phys. Rev. B*, v. 65, p. 195206-5, 2002.

[24] SOUZA, J. A.; RINO, J. P. A molecular dynamics study of structural and dynamical correlation of CaTiO3. *Acta Materialia*, v. 59, p. 1409-1423, 2011.

[25] EVANS, D. J.; HOOVER, W. G.; FAILOR, B. H.; MORAN, B.; LADD, A. J. C.. Nonequilibrium molecular dynamics via Gauss's principle of least constraint. *Phys. Rev. A*, v. 28, p. 1016-1021, 1983.

[26] NOSÉ, S. A unified formulation of the constant temperature molecular dynamics methods. *J. Chem. Phys*., v. 81, p. 511-519, 1984.

[27] BERENDSEN, H. J.; POSTMA, J. P. M.; VAN GUNSTEREN, W. F.; DINOLA, A.; HAAK, J. R. Molecular dynamics with coupling to an external bath. *J. Chem. Phys*., v. 81, p. 3684-3690, 1984.

[28] MORRIS, G. P.; DETTMANN, C. P. Thermostats: Analysis and application. *Chaos*, v. 8, p. 321-336, 1998.

[29] BAKER, G. L.; GOLLUB, H. P. **Chaotic dynamic: an introduction**. Cambridge: Cambridge University Press, 1996.

[30] ECKMANN, J. P.; RUELLE, D. Ergodic theory of chaos and strange attractors. *Rev. Mod. Phys*., v. **57**, p. 617-656, 1985.

[31] ABARDANEL, H. D. I.; BROWN, R.; SIDOROWICH, J. J.; TSIMRING, SH. The analysis of observed chaotic data in physical systems. *Rev. Mod. Phys.,* v. 65, p. 1331-1392, 1993.

[32] GRASSBERGER, P.; PROCACCIA, I. Characterization of strange attractors. *Phys. Rev. Lett.*, v. 50, p. 346-349, 1983.

[33] GRASSBERGER, P.; PROCACCIA, I. Measuring the strangeness of strange attractors. *Physica D*, v. 9, p.189-208, 1983.

[34] TRUELL, R. Ultrasonic Methods and Radiation Effects in Solids. *J. Appl. Phys.*, v. 30, p. 1275-1278, 1959.

[35] TRUEL R.; ELBAUM, C.; CHICK, B. B. **Ultrasonic methods in solid state physics**, New York: Academic Press, 1969.

[36] AULD, B. A. **Acoustic fields and waves in solid**. New York: John Wiley & Sons, 1973.

[37] SCOTT, J. F.; LEDBETTER, H. Interpretation of elasticanomalies in $SrTiO_3$ at 37 K. *Z. Phys. B*, v. 104, 635-639, 1997.

[38] SCHRANZ, W. Dynamic mechanical analysis—a powerful tool for the study of phase transitions. *Phase Transitions*, v. 64, p. 103-114, 1997.

[39] SCHRANZ, W.; SONDERGELD, P., KITYK, A. V.; SALJE, E. K. H. Elastic properties of $SrTiO_3$ crystals at ultralow frequencies. *Phase Transitions*, v. 69, p. 61-76, 1999.

[40] SCHRANZ, W.; TRÖSTER, A.; KITYK, A. V.; SONDERGELD, P.; SALJE, E. K. H. Ultralow-frequency elastic response in $KMn_{1-x}Ca_xF_3$. *Europhys. Lett.*, v. 62, p. 512-518, 2003.

[41] SCHRANZ, W.; SONDERGELD, P., KITYK, A. V.; SALJE, E. K. H. Dynamic elastic response of $KMn_{1-x}Ca_xF_3$: elastic softening and domain freezing. *Phys. Rev. B*, v. 80, p. 094110-12, 2009.

[42] PLIMPTON, S. Fast Parallel Algorithms for Short-Range Molecular Dynamics. *J. Comp. Phys.*, v. 117, p. 1-19, 1995. http://lammps.sandia.gov.

[43] ALI, R.; YASHIMA, M. Space group and crystal structure of perovskite $CaTiO_3$ from 296 to 1720 K. *J. Sol. Stat. Chem.*, v. 178, p. 2867-2872, 2005.

[44] KITTEL, C. **Introduction to solid state physics.** 7th edition, New York: John Wiley & Sons, 1996.

[45] YASHIMA, M.; ALI, R. Structural phase transition and octahedral tilting in the calcium titanate perovskite $CaTiO_3$. *J. Sol. Stat. Ion*., v. 180, p. 120-126, 2009.

[46] BAK, P. **How nature works: The science of self-organized criticality**. New York: Copernicus, 1996.

[47] CASETTI, L.; PETTINI, M., COHEN, E. G. D. Geometric approach to Hamiltonian dynamics and statistical mechanics. *Phys. Rep.*, v. 337, p. 237-341, 2000.

[48] BOFFETTA, G.; CENCINI, M.; FALCIONI, M.; VULPIANI, A. Predictability: a way to characterize complexity. *Phys. Rep.*, v. 356, p. 367-474, 2002.

[49] PACKARD, N. H.; CRUTCHFIELD, J. P.; FARMER, J. D.; SHAW, R. S. Geometry from a Time Series. *Phys. Rev. Lett.*, v. 45, p. 712-716, 1980.

[50] MILLER, S. L.; NASBY, R. D.; SCHWANK, J. R.; RODGERS, M. S.; DRESSENDORFER, P. V. Device modeling of ferroelectric capacitors. *J. Appl. Phys.*, v. 68, p. 6463-6471, 1990.

[51] MILLER, S. L.; SCHWANK, J. R.; NASBY, R. D.; RODGERS, M. S. Modeling ferroelectric capacitor swiching with asymetric nonperiodic input signal and arbitrary initial condictions. *J. Appl. Phys.*, v. 70, p. 2849-2860, 1991.

[52] ANG, C.; BHALLA, A.S.; CROSS, L.E. Dielectric behavior of paraelectric $KTaO_3$, $CaTiO_3$ and $(Ln_{1/3}Na_{1/2})TiO_3$ under a dc electric field. *Phys. Rev. B*, v. 64, p. 1841041-6, 2001.

[53] ANG, C.; YU, Z. dc electric-field dependence of dielectric constant in polar dielectrics: Multipolarization mechanism model. *Phys. Rev. B*, v. 69, p. 174109-8, 2004.

[54] WONG, C. K.; TSUNG, C. H.; SHIN, F. G. Modeling of bias-field-dependent dielectric properties in ferroelectric thin films. *J. Appl. Phys.*, v. 98, p. 074101-9, 2005.

[55] FU, Y. B.; OGDEN, R. W. **Nonlinear elasticity: Theory and applications**. London: Cambridge University Press, 2001.

[56] LIBAI, A.; SIMMONDS, J. G. **The nonlinear theory of elastic shells**. London: Cambridge University Press, 1998.

[57] ANTMAN, S. S. **Nonlinear problems of elasticity**. New York: Springer-Verlag, 1995.

[58] TIKHONOV, A. N.; SAMARSKII, A. A. **Equations of mathematical physics**. New York: Dover Publications, 2011.

[59] BUDAK, B. M.; SAMARSKII, A. A.; TIKHONOV, A. N. **A collection of problems on mathematical physics**. New York: Dover Publications, 2011.

[60] HASSAN, H.; MAGLIONE M.; FONTANA, M. D.; HANDEREK, J. High-frequency dielectric relaxation related to the PE-FE transition in PZT ceramics with low Ti concentration. *J. Phys.: Condens. Matter*, v. 7, p. 8647-8654, 1995.

[61] JOHNSON, K. M. Variation of dielectric constant with voltage in ferroelectrics and its application to parametric devices. *J. Appl. Phys*., v. 33, p. 2826-2831, 1962.

[62] DEVONSHIRE, A. F. Theory of ferroelectrics. *Phil. Mag.*, v. 3**,** p. 85-130, 1954.

[63] RUPPRECHT, G.; BELL, R. O.; SILVERMAN, B. D. Nonlinearity and microwave losses in cubic strontium-titanate. *Phys. Rev.*, v. 123, p. 97-98, 1961.

[64] PLACERES JIMÉNEZ, R., RINO, J. P., FRAYGOLA, B., EIRAS, J. A.. On the capacitance versus voltage response and tunability of ferroelectrics: a microscopic model. *J. Appl. Phys.*, v. 113, p. 074109-8, 2013.

[65] DEFAŸ, E.; LACREVAZ, T.; VO, T. T.; SBRUGNERA, V.; BERMOND, C.; M.; AÏD, FLÉCHET. Ferroelectric properties of Pb(Zr, Ti)O_3 thin films until 40 GHz. *Appl. Phys. Lett.*, v. 94, p. 0529011-3, 2009.

[66] CAO, W.; RANDALL, C. A. Grain size relations in bulk ceramic ferroelectric material. *J Phys. Chem. Solids*., v. 57, p. 1499-1505, 1996.

[67] REN, S. B.; LU, C. J.; LIU, J. S.; SHEN, H. M.; WANG, Y. N.. Size-related ferroelectric-domain-structure transition in a polycrystalline $PbTiO_3$ thin film. *Phys. Rev*. B, v. 54**,** p. 14337-14340, 1996.

[68] KIM, Y.; CHO, Y.; KIM, S.; NO, K. Correlation between grain size and domain size distributions in ferroelectric media for probe storage applications. *Appl Phys Lett*. 89, 162907-3, 2006.

[69] KITTEL, C. Domain Boundary Motion in Ferroelectric Crystals and the Dielectric Constant at High Frequency. *Phys. Rev*., v. 83, p. 458-458, 1951.

[70] ARLT, G.; PERTSEV, N. A.. Force constant and effective mass of 90° domain walls in ferroelectric ceramics. *J. Appl. Phys*., v. 70, p. 2283-2889, 1991.

[71] PERTSEV, N. A.; ARLT, G.. Forced translational vibrations of 90° domain walls and the dielectric dispersion in ferroelectric ceramics. *J. Appl. Phys*., v. 74, p. 4105-4112, 1993.

[72] ARLT, G.; BÖTTGER, U.; WITTE, S. Emission of GHz shear waves by ferroelstic domain walls in ferroelectrics. *Appl. Phys. Lett*., v. 63, p. 602-604, 1993.

[73] LI, S.; CAO, W.; CROSS, L. E. The extrinsic nature of nonlinear behavior observed in lead zirconate titanate ferroelectric ceramic. *J. Appl. Phys.,* v. 69, p. 7219-7224, 1991.

[74] MALKIN, I. G. **Some problems in the theory of nonlinear oscillation**. Washington: United State Atomic Energy Commission, 1959.

[75] ELSGOLTZ, L. **Ecuaciones diferenciales y cálculo variacional**. Moscow: Mir, 1969.

[76] JONSCHER, A. K. The ‘universal’ dielectric response. I. *IEEE Electr. Insul. Mag.*, v. 6, 16-22 (1990).

[77] JONSCHER, A. K. The ‘universal’ dielectric response. II. *IEEE Electr. Insul. Mag*., v. 6, p. 24-28, 1990.

[78] KLIEM, H. Dielectric small-signal response by protons in amorphous insulators. *IEEE Trans. Electr.Insul*., v. 24, p. 185-197, 1989.

[79] KLIEM, H.; KUEHN, M. Modeling the switching kinetics in ferroelectrics. *J. Appl. Phys*. v. 110, p. 114106-5 (2011).

[80] PLACERES JIMÉNEZ, R.; ZAYAS, F. G.; M’PEKO, J. C.; Erias, J. A.. A numerical study of relaxation in a two dimensional dipolar lattice. *J. Appl. Phys*., v. 99, p. 064102-4 (2006).

[81] PLACERES JIMÉNEZ, R.; ZAYAS, F. G. Relaxation and hysteresis in a two-dimensional dipolar lattice. *Phys. Rev. B*, v. 73, p. 174304-5, 2006.

[82] PAKHOMOV, A.; LUK’YANCHUK, I.; SIDORKIN, A.. Frequency dependence of the dielectric permittivity in ferroelectric thin films with 180° domain structure. *Ferroelectrics,* v. 444, p. 177-182, 2013.